VRIJE UNIVERSITEIT AMSTERDAM

UNIVERSITY OF AMSTERDAM
Institute of Physics

Master Thesis

Scaling Up the Future:
Large Area Exfoliation of 2D materials for Heterostructure Fabrication

by

Sabyasachi Phukan

(UvA student number – **13601156**)

Supervisor: **Prof. Dr. Peter Schall**

Daily supervisors: **Marco van der Laan** & **Tom Hoekstra**

Second Examiner: **Dr. Jorik van de Groep**

Submitted in fulfilment of the requirements for the joint UvA-VU degree of Master of Science in Physics and Astronomy: Science for Energy and Sustainability

Contents

Acknowledgements

I would like to extend my sincere gratitude to Prof. Dr. Peter Schall and Marco van der Laan for granting me the opportunity to embark on this incredible project. From the very beginning, Peter's unwavering belief in my work strongly encouraged me to achieve our shared goals. His support also created an environment where I felt empowered to take risks and embrace creativity. Marco's invaluable guidance and support in various aspects, including experimental techniques, data analysis, presentation skills, and academic writing, have enriched my journey as a researcher. I am truly fortunate to have had him as my mentor, and his expertise has significantly helped me deepen my understanding of the topic as he answered my numerous questions.

I would like to express my sincere appreciation to Dr. Jorik van de Groep and Tom Hoekstra, whose contributions were integral to the success of this project. Without their assistance and timely interventions, I would not have been able to achieve our research objectives. Jorik's expertise and support in this project have been invaluable, and I am grateful for the opportunity to collaborate with Tom, which has taught me the importance of effective teamwork. I would also like to thank Dr. Thomas Bauer for his generous assistance, sharing his knowledge on the 2D materials we investigated, and providing crucial insights that guided me in evaluating the quality of my samples.

Lastly and again, I extend a special thanks to Tom Hoekstra for his exceptional work in fabricating the gold foil and also partially supervising my work along with Marco in the later stages of the project.

Abstract

Monolayers of two-dimensional transition metal dichalcogenides (2D TMDCs) such as those of MoS_2 and WS_2 offer a promising alternative to the use of Si in solar energy harvesting and other applications due to their direct bandgaps, high absorption efficiency, and their ultralight and flexible nature. For device applications, such monolayers need to be of large area and high quality. Most top-down and bottom-up fabrication methods have failed to produce such monolayers that are simultaneously large and of high quality. This project focuses on using a method known as "gold-assisted exfoliation" that enables the top-down fabrication of these monolayers over large areas. We characterize the monolayers using Raman spectroscopy and asses their quality by studying their optoelectronic behavior using photoluminescence spectroscopy. We extend the gold-assisted exfoliation method from MoS_2 and WS_2 further to ReS_2 and $ReSe_2$, to obtain their monolayers, focusing primarily on assessing the reproducibility of the fabrication method. The results demonstrate that the gold-assisted exfoliation method enables the production of large-area monolayers with sizes spanning more than $2\ mm \times 2.5\ mm$ in area, and with quality close to that of pristine MoS_2 and WS_2 monolayers. These monolayers can be transferred from gold to other substrates for heterostructure fabrication. We specifically explored MoS_2/WS_2 heterostructures which we successfully fabricated using this method. This work contributes to the development of efficient and scalable methods for fabricating semiconducting TMDC monolayers and heterostructures, paving the way for their reliable use in various device applications.

List of Commonly Used Abbreviations

1. **Al_2O_3:** Aluminum Oxide (Alumina)
2. **Au:** Gold
3. **CBM:** Conduction Band Minimum
4. **CLQB:** Covalent-like Quasi Bonding
5. **CVD:** Chemical Vapor Deposition
6. **FWHM:** Full Width at Half Maximum
7. **GAE:** Gold Assisted Exfoliation
8. **ML:** Monolayer
9. **Mol. W:** Molecular Weight
10. **MoS_2:** Molybdenum Disulfide
11. **PDMS:** Polydimethylsiloxane
12. **PL:** Photoluminescence
13. **PMMA:** Poly(methyl methacrylate)
14. **PVP:** Polyvinylpyrrolidone
15. **ReS_2:** Rhenium Disulfide
16. **$ReSe_2$:** Rhenium Diselenide
17. **Si:** Silicon
18. **SiO_2:** Silicon Dioxide
19. **TMDC:** Transition Metal Dichalcogenide
20. **TRT:** Thermal Release Tape
21. **VBM:** Valence Band Maximum
22. **WS_2 :** Tungsten Disulfide

Chapter 1

Introduction

Climate change has created an urgent need for rapid advancements in renewable energy technologies, with solar energy being a key solution to meet global energy demands. Material science, particularly the field of light-matter interactions, plays a pivotal role in enabling the development of highly efficient and cost-effective solar energy harvesting technologies. Silicon (Si), a conventional semiconducting material, has dominated the photovoltaics industry with a global market share of around 95% in 2021 [1]. This figure has not much changed since then. However, the indirect bandgap of Si limits the efficiency of the light absorption process which restricts the possibility of thinning down the material below 100 μm to achieve flexible and lightweight structures [2,3]. In contrast to silicon, monolayers of two-dimensional layered transition metal dichalcogenides (TMDCs), including molybdenum disulphide (MoS_2) and tungsten disulphide (WS_2) possess direct bandgaps which facilitate highly efficient light absorption. Additionally, these ultrathin materials offer high flexibility and lightweight properties due to their monolayer thickness of less than 1 nm [4,5]. These qualities make TMDC monolayers promising for various practical applications including photodetection, photovoltaics and photocatalysis. Moreover, due to strong spin-orbit coupling and lack of inversion symmetry in these materials, they are largely explored for valleytronics, and spintronics [6–8]. Assembly of these monolayers into heterostructures can further enhance light absorption over a wider spectral range and also help in charge separation and collection processes, providing even greater potential for these materials [9].

However, certain challenges have hindered the fabrication of large high-quality TMDC monolayers. While some top-down methods, such as mechanical exfoliation using scotch tape, have succeeded in producing high-quality, defect-free monolayers, the extremely small monolayer size remains a significant obstacle to large-scale application [10]. Conversely, methods have produce large-area monolayers, such as chemical vapor deposition (CVD), often result in high number of defects, which also negatively impacts their efficiency and reliability for device applications [11]. These challenges in obtaining large high-quality monolayers further makes it difficult to fabricate high-quality heterostructures that could be implemented in a device [12].

In this project, we aim to overcome these challenges by employing the gold-assisted mechanical exfoliation (GAE) method. Gold atoms form covalent-like quasi-bonding (CQLB) with the chalcogen atoms of the TMDC monolayers. If the gold foil is atomically smooth, it enables large-area mechanical exfoliation of these monolayers [13]. This is crucial in achieving our primary objectives of

fabricating monolayers with **i)** *large area;* and **ii)** *high quality*; as well as fabricating **iii)** *heterostructures* using these monolayers [14]. We use confocal microscopy and Raman spectroscopy to identify and characterize these monolayers, and photoluminescence (PL) spectroscopy to assess their quality. We further compare the quality of the monolayers to samples fabricated through the CVD method as well as to small area monolayers of pristine quality fabricated through mechanical exfoliation using Scotch-tape.

In this thesis, we first present the fundamental physics associated with the optoelectronic properties of the 2D TMDC monolayers we investigated, in Chapter 2. This includes concepts related to their crystalline structure, electronic band structures, excitonic properties and vibrational properties. These concepts enable us to understand the rationale behind the parameters we used in this project to characterize these materials and evaluate their quality. Within the same chapter, we further provide a brief discussion on the optoelectronic properties of the heterostructures in the context of this project, and end it with a short note on why we preferred the method of gold-assisted exfoliation.

Chapter 3 discusses the experimental methods used for fabricating the ultrasmooth gold foil, followed by the gold-assisted exfoliation of the 2D TMDCs and the fabrication of heterostructures. We finally end this chapter by discussing the Lorentz function fitting procedure, which we used for analyzing data from the Raman and PL spectra for characterization and quality evaluation.

We then present and discuss our results in Chapter 4. In this chapter, we first show that using the GAE method, we are able to exfoliate monolayers of sizes more than $2\ mm\ \times 2.5\ mm$ in area, followed by characterizing their behavior on and off gold. Then we present a discussion on how our fabricated samples are of better quality as compared to commercially available CVD samples using parameters extracted from the PL spectra. Finally in this chapter, we briefly discuss the results for the MoS_2/WS_2 heterostructures we fabricated using the GAE method, where we speculate that the coupling between the two individual monolayers may not be high enough to enable efficient charge transfer between them.

In chapter 5, we end our thesis by summarizing our main findings and also providing an outlook towards future research ideas which are possible due to the success of this fabrication method. We acknowledge that there are certain limitations to this method which might hinder the fabrication of high-quality heterostructures with efficient charge transfer mechanism, but with further optimizations in the fabrication process, these limitations can be overcome.

Chapter 2

Background

2.1 Crystal and Band structure

2.1.1 Crystalline Structure of 2D TMDCs

The general chemical formula for 2D TMDCs is MX_2, where 'M' denotes a transition metal atom (such as Mo, W, or Re) and 'X' represents chalcogen atoms (such as S or Se). These materials consist of a plane of 'M' atoms sandwiched between two hexagonal planes of 'X' atoms in the form X-M-X **(Figure 2.1)**. The oxidation state of the 'M' atom is +4, while the 'X' atoms exhibit an oxidation state of -2. In each individual layer, there is strong in-plane covalent bonding among the metal (M) and chalcogen atoms (X), while vertically, the adjacent layers are held together by weak van der Waals forces. This enables the facile cleavage of the bulk version of these materials using either mechanical or chemical methods, resulting in individual two-dimensional monolayers [15].

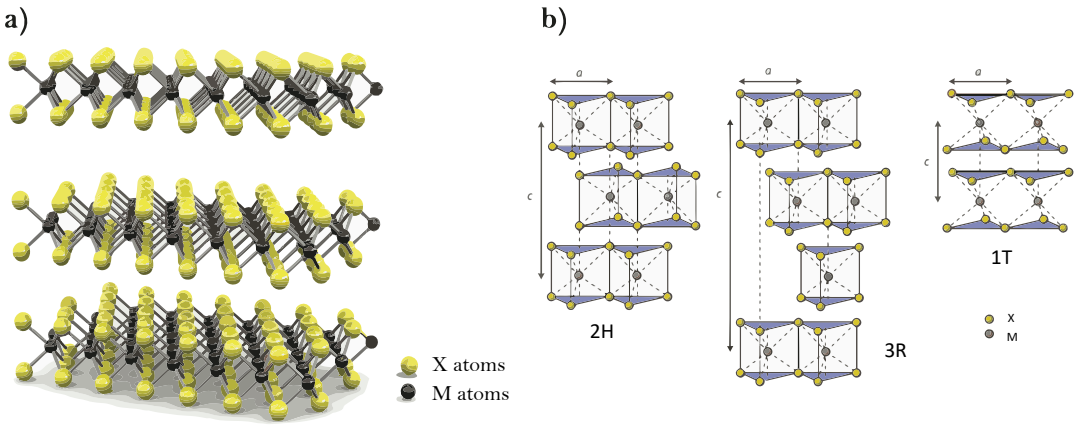

Figure 2.1: a) Three dimensional schematic view of three MX_2 monolayers in X-M-X configuration [94]; **b)** Three different structural polytypes of TMDCs: 1T (Tetragonal symmetry with 1 layer per repeat unit, Octahedral coordination), 2H (Hexagonal symmetry with 2 layers per repeat unit, Trigonal Prismatic coordination), 3R (Rhombohedral symmetry with 3 layers per repeat unit, Trigonal Prismatic coordination) [22]

In their bulk form, the 2D TMDCs, investigated in this project, exist in three major structural polytypes: 1T, 2H and 3R [16] (**Figure 2.1, b)** above). "T", "H" and "R" refers to Tetragonal, Hexagonal and Rhombohedral symmetry respectively. The numbers represent the amount of layers in a single repeat unit in these symmetries. The two main coordinations are "Trigonal Prismatic",

also known as 2H coordination, or 1H in the limit of a monolayer, and "Octahedral", also known as 1T coordination, associated with point groups D_{3h} and D_{3d} respectively [17].

MoS_2 and WS_2, can exist in both 1T and 1H polytypes. However, we only investigate the 1H polytype in this project, which are semiconductors, while 1T polytypes are metallic[18]. In addition, we explore the possibility of employing our method to the Group-VII TMDCs, ReS_2 and $ReSe_2$ which display a distorted 1T-phase commonly referred to as the 1T'- (or distorted octahedral) phase. This distortion is known as Peierls distortion and it arises from the inclination of Re atoms to engage in covalent bonding with neighboring Re atoms as a means of reducing energy [19]. Typically, the 1T-phase of ReX_2 (X: S or Se) is metallic in nature with the Fermi-energy level crossing a partially occupied orbital. However, due to Peierls distortion, a bandgap is introduced into the material, resulting in its semiconducting behavior [19] .

2.1.2 Brillouin Zone in 2D TMDC Monolayers

The Brillouin zones of these monolayer crystals are hexagonal in nature and have high symmetry points located at the corners ($\boldsymbol{K-point}$ and $\boldsymbol{-K-point}$), at the midpoint between $K-point$

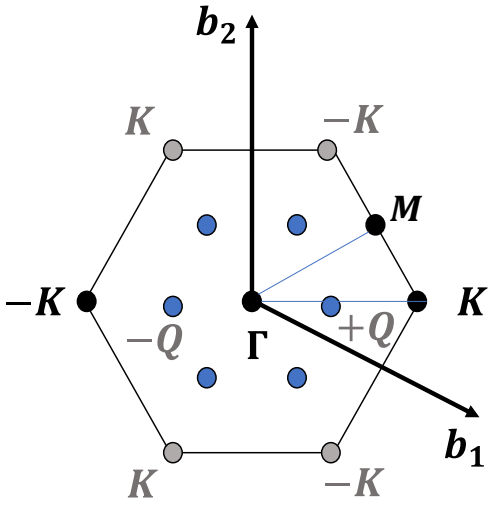

Figure 2.2: The first 2D hexagonal Brillouin zone for the 2D crystals. $\boldsymbol{b_1}$ and $\boldsymbol{b_2}$ are reciprocal lattice vectors [24]. (Modification and placing of the low symmetry Q-points from [23]).

and $-K-point$ ($\boldsymbol{M-points}$), and at the center ($\boldsymbol{\Gamma-point}$) as shown in **Figure 2.2**. Furthermore, the stacking of individual monolayers enhances their electronic and vibrational coupling in the out-of-plane direction thereby increasing the significance of the low symmetry $\boldsymbol{Q-points}$ and $\boldsymbol{-Q-points}$ for indirect electronic transitions in the *k-space* [20,21].

The density of electronic energy states available at and around each of these symmetry points in the momentum space forms the electronic band structures – *the correlation between the energy and momentum of an electron in these materials.* Band structures offer valuable insights into the optoelectronic behavior of different materials and can be obtained using advanced computational techniques like density functional theory (DFT) and tight-binding models, as well as experimental methods like angle-resolved photoemission spectroscopy (ARPES).

2.1.3 Electronic Band Structures of MoS_2 and WS_2

As Group-VI TMDCs like MoS_2 and WS_2 transition from bulk to monolayer, a significant change occurs in their band structure which transforms their bandgap from indirect to direct (**Figure 2.3**) [22–25]. In bulk, electronic transitions occur from the valence band maximum (VBM) at the $\Gamma - point$ to the Conduction Band Minimum (CBM) at the $Q - point$, requiring an extra amount of momentum for an electron to make this transition. However, in monolayers, this transition occurs from the VBM at $K - point$ to the CBM at $K - point$, without the need for additional momentum. This significantly increases the probability of these electronic transitions occurring. Additionally, the bandgap increases from around 1.2 eV to 1.8 eV for MoS_2 and from 1.3 eV to 2.1 eV for WS_2 going from bulk to monolayer [22]. These two materials have similar band structures due to their comparable crystal structures and composition.

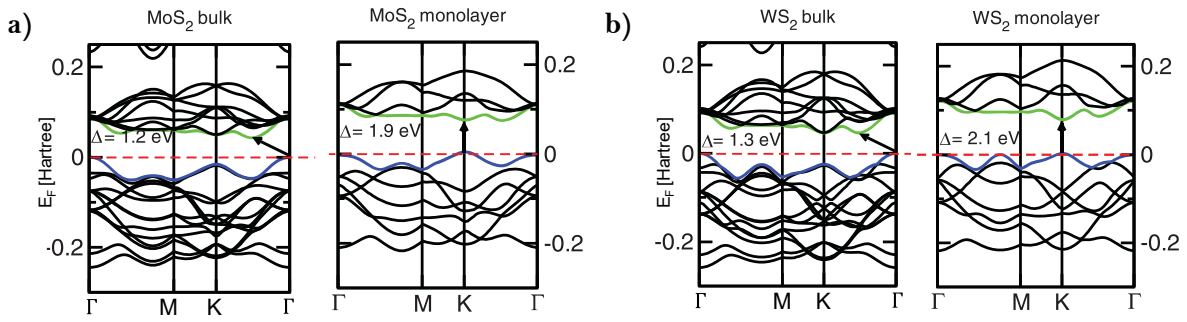

Figure 2.3: a),b) *ab-initio* DFT calculated band structures for bulk and monolayer versions of MoS_2 (**a)**) and WS_2 (**b)**). Red dashed lines indicate the Fermi-level in both the materials [25].

The indirect-to-direct bandgap transitions in these semiconductors can be explained by considering the electronic energy states near the $\Gamma - point$ in the Brillouin Zone. These states have orbitals that are linear combinations of the p_z-orbitals of the S-atoms and d_{z^2}-orbitals of the M (Mo or W) atoms, which are delocalized and anti-bonding in nature. As the interlayer distance increases in the out-of-plane (z-)direction, the interlayer interaction decreases, resulting in a reduction in energy of these anti-bonding orbitals. Conversely, electronic energy states around the $K - point$ have orbitals localized in the x-y plane and are therefore not affected by changes in the interlayer distance in the z-direction [26]. Thus, while the energy of the indirect transition around the $\Gamma - point$ increases with

reduced layer thickness, the energy of the direct transition, at the $K-point$, is less affected. This results in the indirect-to-direct bandgap crossover going from bulk to monolayers.

The monolayers of these materials also exhibit another important feature which is the splitting of the VBM and CBM at the K and $-K\ points$ [27,28]. This splitting is a consequence of spin-orbit coupling and is depicted in **Figure 2.4 a)** and **b)**. The band-splitting leads to the presence of two distinct electronic transitions, namely A- and B-excitonic transitions which are of different spins. [29].

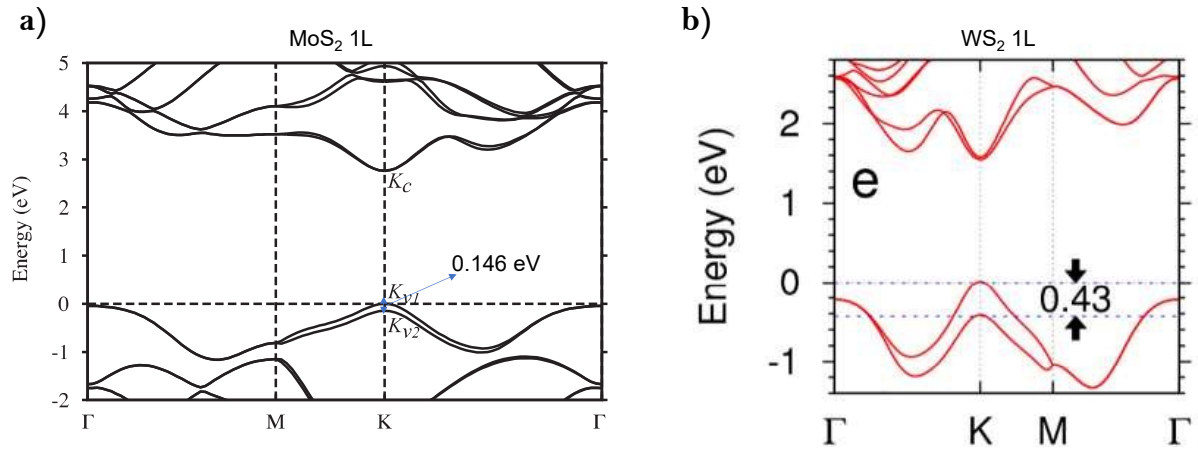

Figure 2.4: Band-splitting in monolayers of **a)** MoS_2; and **b)** WS_2 due to spin-orbit coupling [27,28]

The band-splitting is more significant in WS_2 than in MoS_2, primarily due to the stronger spin-orbit coupling resulting from the greater mass of the tungsten (W) atom. For a brief overview of the band structures of Group VII TMDCs (ReS_2 and $ReSe_2$), we refer to **Appendix A1**.

2.2 Why Gold-Assisted Exfoliation?

In our study, we successfully obtained monolayers of MoS_2 and WS_2 using the gold-assisted exfoliation (GAE) method. This allowed us to overcome the challenges associated with obtaining large-area and high-quality samples. Such samples were previously difficult to fabricate using other top-down methods such as mechanical exfoliation and bottom-up approaches such as CVD. The key factor enabling this process is the strong interaction between the gold layer and the monolayers, often referred to as covalent-like-quasi-bonding (CLQB) [30–32]. This interaction, which lies between covalent bonding and van der Waals interaction in terms of strength, facilitates the easy separation

of the monolayers from the bulk crystal when they come into contact with the gold layer, as depicted in **Figure 2.5 a).**

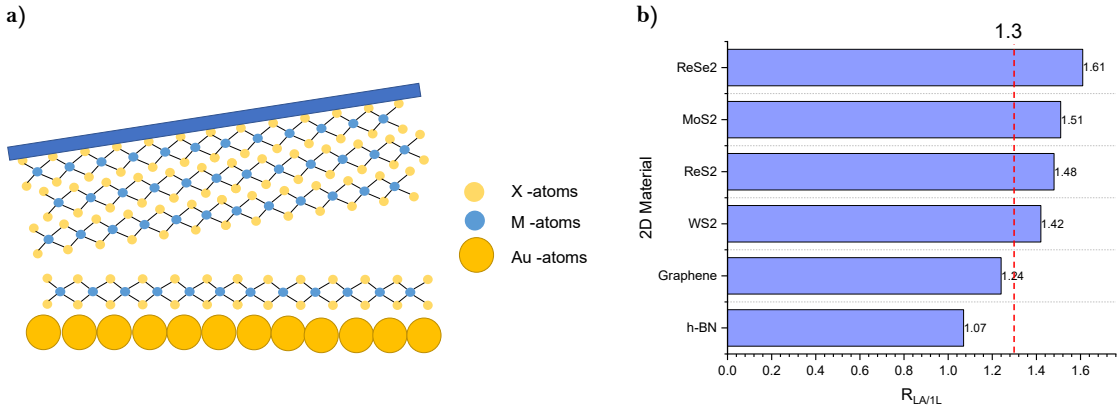

Figure 2.5: a) Schematic for gold-assisted exfoliation method facilitated by the CLQB interaction between the gold-atoms and the TMDC monolayer in contact with it; **b)** $R_{LA/1L}$ values for different 2D materials including the ones we exfoliated in our project. Values taken from [30].

CLQB interactions are particularly favorable for metallic substrates with partially filled s- or p-orbitals, as these materials do not disrupt the electronic band structure of the 2D layers by strongly hybridizing with their orbitals. Additionally, they possess highly polarizable electron densities, promoting large dispersion attractions [67]. Noble metals such as Au, Cu, and Ag are suitable candidates for this type of interaction, with Au being the most promising due to its low chemical reactivity and air-stability [30].

Using DFT calculations and experimental techniques, Huang *et al.* determined the ratio of interaction energies between individual layers of the 2D material and between a single layer of the 2D material and gold ($R_{LA/1L}$) [30]. Materials with an $R_{LA/1L}$ ratio greater than 1.3 were found to be suitable for exfoliation using this method. **Figure 2.5 b)** illustrates the $R_{LA/1L}$ values for various materials, demonstrating that the materials investigated in our study had values exceeding 1.3, indicating their high compatibility with the GAE method. Conversely, materials like graphene and hexagonal-Boron Nitride (h-BN) are less suitable for exfoliation using this approach. Thus, using this method, it is possible to exfoliate many more 2D materials that have $R_{LA/1L}$ values more than 1.3.

However, one of the major limitations of this method is its ineffectiveness with prolonged exposure of the gold foil to ambient atmosphere. For optimal monolayer yield, the exfoliation process needs to be carried out within 5-6 minutes in order to avoid contamination on the surface of the gold foil which would compromise the contact between the gold and the monolayer. Another limitation is the requirement of a smooth and ultra-flat gold layer that would enable optimal contact between the

monolayer and the gold atoms. Within these constraints, it is possible to obtain large-area monolayers on the gold foil using the GAE method as will be shown in section **3.2.2**.

2.3 Excitons

Excitons are charge-neutral quasiparticles composed of an electron and a hole that are bound together by attractive Coulomb interactions. They are formed in insulators and semiconductors when an electron absorbs energy, becomes excited to a quantized energy state below the conduction band continuum, and leaves behind a hole in the valence band. The excited state spectra of these quasiparticles can be described by an "excitonic Rydberg series", similar to the hydrogen series. The electron and hole's attraction and separation are determined by a balance between their Coulomb forces, the electric field screening of the excited electron by surrounding electrons, and the effective masses of the electron and hole. As excitons are bound to each other, they have less energy than free electrons and holes [33,34].

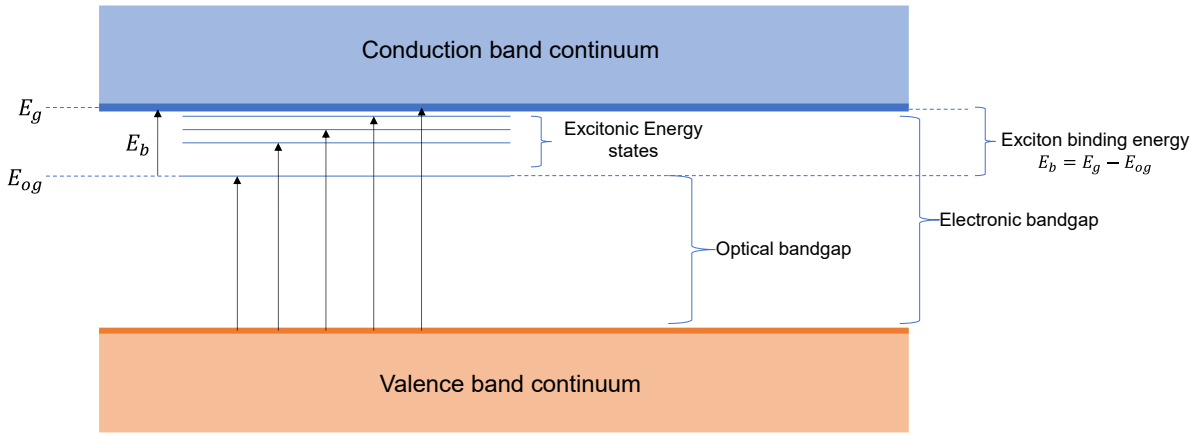

Figure 2.6: Schematic representation of electronic transitions in semiconductors. Schematic inspired from [34].

The strength of the Coulomb interaction between the electron and hole determines the exciton's binding energy (E_b) - *the minimum energy required to dissociate the exciton into free charges.* The exciton binding energy is also defined as the energy difference between the conduction band continuum and the energy level at which the electron resides in the excitonic configuration. **Figure 2.6** is a schematic of the various electronic transitions that might lead to the formation of excitons and free charges. The exciton binding energy can be expressed as

$$E_b = E_g - E_{og} \tag{2.3}$$

where E_g and E_{og} refers to the electronic and optical bandgap in the material respectively. The optical bandgap is the minimum photon energy that can be absorbed by the material [35].

2.3.1 Excitons in 2D TMDCs

In 2D TMDCs, due to the lack of surrounding material, the dielectric screening of the excitons is reduced. In essence, in the monolayer limit, the Coulombic interactions between the electron and the hole is screened only in the in-plane direction, while the electric field lines between the pair can exist almost unaffected in the out-of-plane direction, provided it is a free-standing monolayer in vacuum **(Figure 2.7 a))** [36]. This reduced screening of the Coulombic interaction between them, and also quantum confinement of the electron in the plane of the layered material thereby increases the excitonic binding energy [36,37].

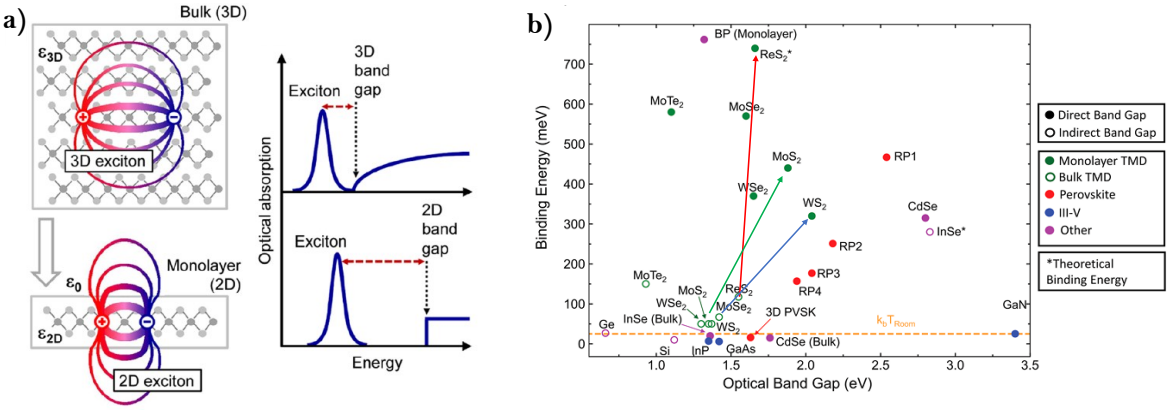

Figure 2.7: a) Plot of binding energy versus optical bandgaps for semiconductors in bulk and monolayer form . Arrows indicate the increase in binding energies with dimensionality reduction for TMDCs studied in this project [37]; **b)** Increased Coulombic interaction between electron-hole pairs on dimensionality reduction due to reduced dielectric screening [36]

Thus, the excitonic features of 2D TMDC monolayers can be observed even at room temperatures with binding energies of hundreds of meV [38]. The increase in the exciton binding energy due to the reduction in dimensionality can be roughly estimated using

(2.3.1)

$$\frac{E_{b(2D)}}{E_{b(3D)}} = \frac{n^2}{\left(n-\frac{1}{2}\right)^2}$$

where n $(= 1,2,3 \ldots)$ is the energy level in the excitonic Rydberg series. Thus, for the ground state, the binding energy increases roughly by a factor of 4 [39]. **Figure 2.7 b)** depicts the increase in the values of binding energy as the dimensionality is reduced for MoS_2 (*green arrow*), WS_2 (*blue arrow*) and ReS_2 (*red arrow*).

2.3.2 Types of Excitons in 2D TMDCs

In monolayers of 2D TMDCs, the interaction between electrons and the crystal lattice gives rise to diverse excitonic configurations. These configurations can be broadly classified into "bright" and "dark" excitons, depending on the type of allowed electronic transitions based on energy, momentum and spin conservation laws. Bright excitons involve electron-hole pairs that have higher radiative recombination rates while for dark excitons the probability to recombine radiatively is much lower. Additionally, more complex configurations can arise, involving the simultaneous presence of three or more electrons, leading to the formation of biexcitons and trions. In this section, we provide an intuitive understanding of excitonic configurations, shedding light on their distinct properties.

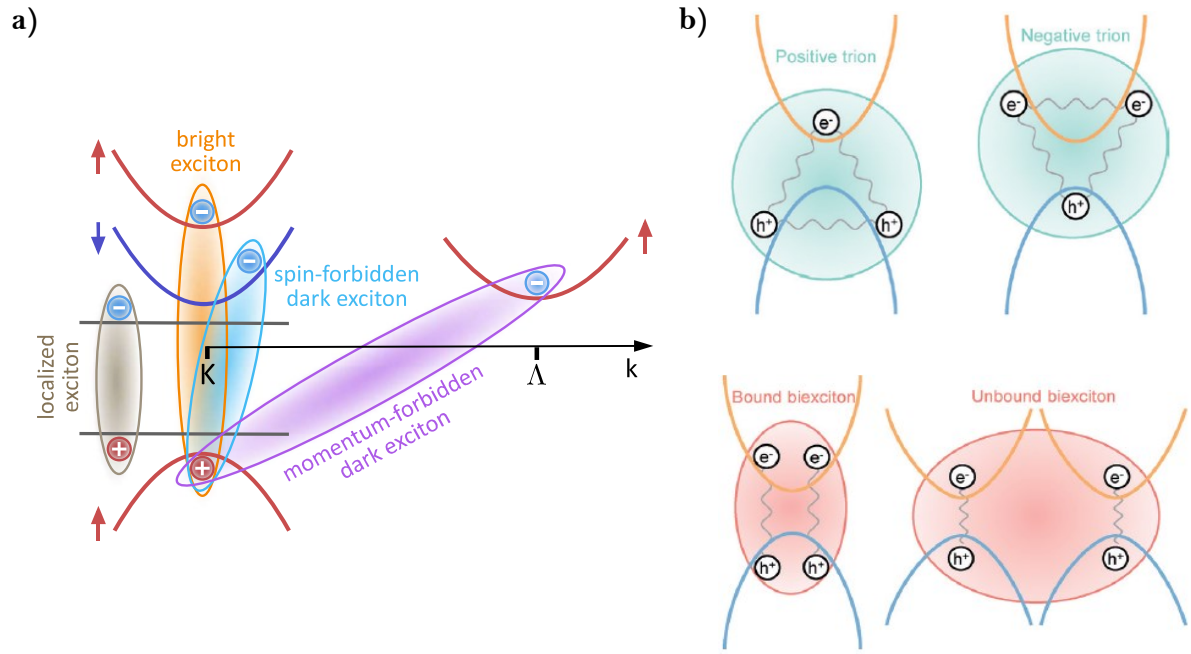

Figure 2.8: **a)** Schematic for bright and dark excitonic configurations in 2D TMDCs [40]; **b)** Schematic for trions (above) and biexciton (below) configurations [35]

2.3.2.1 Bright, Dark and Localized Excitons

Bright excitons in monolayers of 2D TMDCs are characterized by an excited electron and a hole occupying the same symmetry point in the momentum space and having the same spin angular momentum. The excited electron emits a photon with energy equal to the difference between the excited energy state it occupied below the conduction band continuum and the VBM, resulting in energy loss and recombination with the hole [40]. This process of radiative recombinations by emitting a photon is also known as photoluminescence, provided the electron was excited by another photon. This is described in detail in section **2.2.4**.

However, if the electron and hole have different momenta, the probability of radiative recombination by photon emission is much lower. In this case, the electrons in these excitonic complexes need to acquire or lose momentum prior to recombination and hence are known as momentum-dark excitons. Additionally, if the difference in spin between the ground- and excited state of the electron differ more than what can be bridged by a photon, the probability of radiative recombination is again significantly diminished as the electron needs to scatter to the other states before the recombination process. This extends to exciton states and these complexes are hence termed spin-dark excitons. **Figure 2.8 a)** presents a schematic representation of the various types of excitons encountered in monolayers of 2D TMDCs, illustrating their distinct characteristics [40].

Localized excitons are formed when energy states in the bandgap become available due to the presence of defects. These trapping potentials may be formed due to atomic vacancies of the metal or the chalcogen atoms, or due to strain. Their effect becomes important in low-temperature regime. However, at room temperatures, the thermal energy of the excitonic pair is typically high enough to overcome this local potential well [40].

2.3.2.2 Other Excitonic Complexes

When the material contains free charge carriers or under high excitation fluences, the excitons can become Coulombically bound to one of the charge carriers, resulting in the formation of charged trions [35]. A trion can be either negatively charged, where the exciton binds with an additional electron, or positively charged, where it binds to an extra hole (as depicted in **Figure 2.8 b)**). These trionic complexes have been experimentally observed and studied, revealing their unique electronic properties [41].

Furthermore, two excitons can interact with each other, leading to the formation of biexcitons - *excitonic complexes with Coulomb interactions between two excitons.* These biexcitons can be of two categories: **i)** bound biexcitons, which exhibit attractive Coulombic interactions, and **ii)** unbound biexcitons, which involve repulsive Coulombic interactions between the two excitons, both being stable at room temperature [35]. The existence of these biexciton complexes was first experimentally observed in 2D TMDCs based on tungsten [42,43]. The exploration of these various excitonic complexes provides valuable insights into the rich physics and non-linear optical properties of 2D TMDC materials.

We experimentally tried to observe such complexes under high excitation flux in our monolayers of MoS_2 and WS_2. The results are provided in the **Appendix A3**. Although we could observe trions, we could not identify the formation of biexcitons.

2.3.3 Photoluminescence

Photoluminescence (PL) is the process of absorbing photons or electromagnetic radiation by a material and subsequently re-emitting photons. **In Figure 2.9,** a schematic representation illustrates this process where high-energy photons, surpassing the bandgap energy, excite an electron from the valence band to the conduction band leaving behind a hole in the valence band. Following this initial excitation, the electron and hole loose energy via thermalization, caused by electron-phonon interactions, reaching the CBM and the VBM respectively by conserving energy and momentum and thereby forming an exciton. Eventually, the electron and hole recombine, resulting in the emission of a photon with energy equivalent to the optical bandgap of the material.

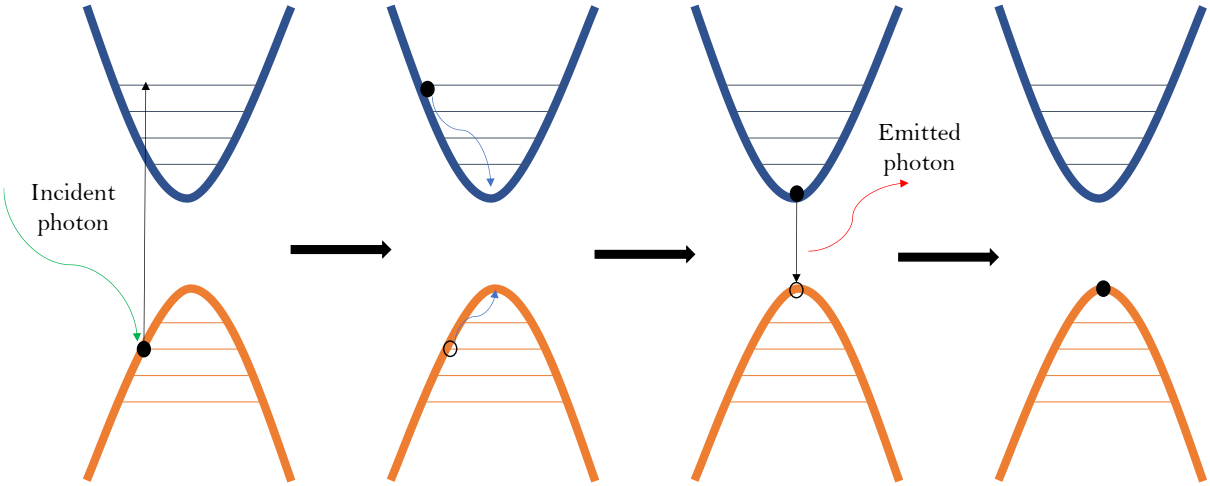

Figure 2.9: Schematic showing the PL process in direct bandgap semiconductors. The black filled circle represents an electron and the unfilled circle represents a hole.

A crucial metric for assessing the efficiency of the radiative recombination process is the PL quantum yield (PLQY) [44,45]. It can be defined as the ratio of emitted photons ($N_{Photons\ emitted}$) to absorbed photons ($N_{Photons\ absorbed}$), and can be expressed as:

$$\text{PLQY} = \frac{N_{Photons\ emitted}}{N_{Photons\ absorbed}} = \frac{k_r}{k_r + \Sigma k_{nr}} \leq 1 \qquad (2.3.3)$$

where k_r and k_{nr} refer to the radiative and non-radiative recombination rates in the material respectively. Lower PLQY indicates the presence of non-radiative recombination pathways, which can be induced by, for example defects and impurities within the material. The consequences of these non-radiative processes become evident when examining the material's PL spectra—*a plot showing the number of photons emitted at various energies or wavelengths.*

Ideally, the PL spectra of the materials investigated in this project should exhibit a narrow peak at energies corresponding to the material's optical bandgap. However, due to the presence of non-

radiative decay pathways, the PL peak tends to broaden around the optical bandgap energy [46]. Additionally, the number of emitted photons decreases specifically at this energy. These characteristic changes causes the radiative recombination to decrease, emphasizing the impact of non-radiative mechanisms on the material's photoluminescent properties [47,48]. In this study, we considered these characteristics to determine the quality of the materials fabricated.

2.3.4 Exciton Decay Dynamics in 2D TMDCs

Following the formation of excitons, their subsequent decay can occur through radiative or non-radiative processes, resulting in multiexponential decay channels [49]. In radiative recombination, excitons release energy by emitting photons while obeying the laws of momentum and energy conservation. However, excitons can also undergo non-radiative recombination without photon emission, involving mechanisms such as defect-assisted recombination, exciton-phonon interactions, and surface/interface effects [49]. In some cases, when the lowest-lying exciton is a dark exciton, as observed in certain tungsten-based TMDCs, non-radiative recombination becomes the dominant decay pathway [49,50]. Additionally, environmental factors such as temperature, laser fluence, and dielectric environment can also influence the recombination process [50].

To illustrate this, Shi *et al.* measured the population decay dynamics using transient absorption spectroscopy on suspended monolayers of MoS_2 [51]. The experimental decay curve was fitted with three exponential decay functions convoluted with a Gaussian Response Function (GRF) according to

$$f \propto \left(Ae^{-t/\tau_1} + Be^{-t/\tau_2} + Ce^{-t/\tau_3}\right) * (GRF) \qquad \textbf{(2.3.4)}$$

The fitting suggests that the decay processes were characterized by three time constants: fast (around $\tau_1 = 2.6$ ps), intermediate (around $\tau_2 = 74$ ps), and slow (around $\tau_3 = 850$ ps). The fast and intermediate decay processes were attributed to the presence of defects, impurities, and substrate effects, leading to rapid non-radiative recombinations. Conversely, the slow decay process was associated with radiative recombination. The competition between radiative and non-radiative decay pathways serves as an indicator of material quality in the context of materials investigated in this project. Higher non-radiative pathways indicate lower material quality. **Figure 2.10** shows

various relaxation or decay pathways for excitons which are mainly divided into radiative and non-radiative recombination processes.

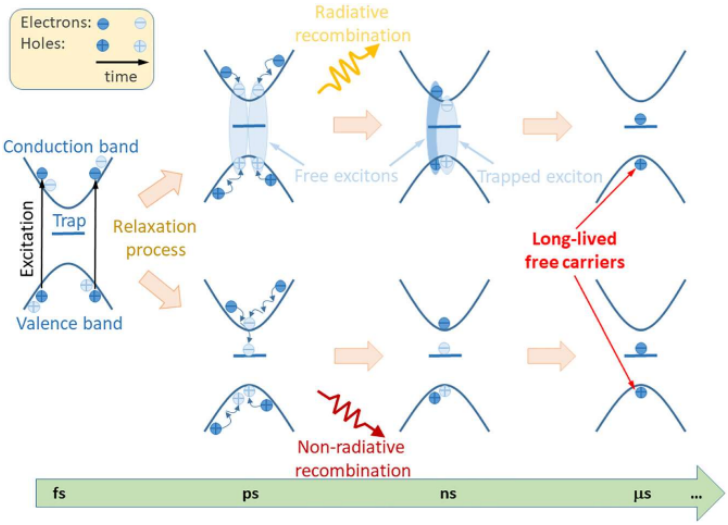

Figure 2.10: Exciton decay process in monolayers of 2D TMDCs [95].

2.4 Raman Spectroscopy of 2D TMDCs

2.4.1 Raman Scattering

Raman spectroscopy is an experimental technique that plays a crucial role in identifying the molecular vibrational and rotational energy modes present in a material. By subjecting molecules or materials to light or electromagnetic radiation, a separation between their electron clouds and nuclei

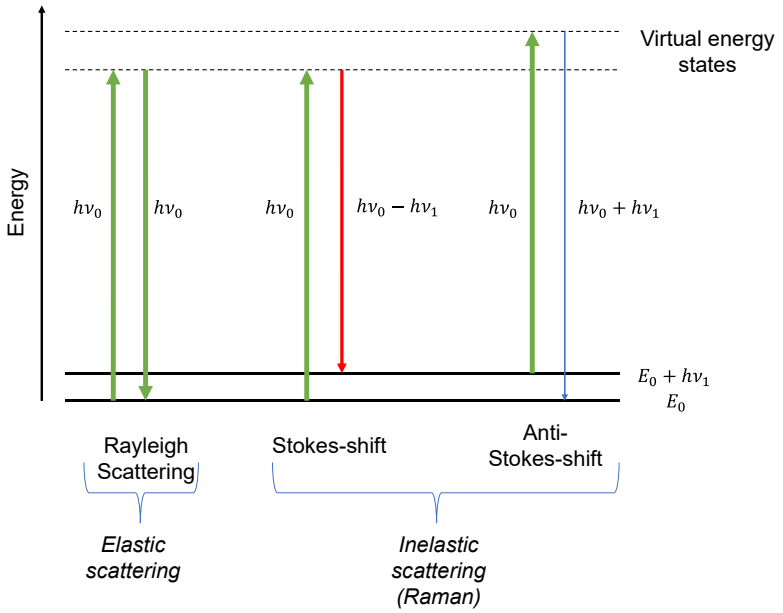

Figure 2.11: Schematic for elastic and inelastic scattering of green laser light. The inelastic scattering shown here is essentially the Raman scattering in these materials.

is induced. This separation leads to the generation of a dipole moment and the excitation of electrons from a ground vibrational state to virtual energy states. In this process, a significant portion of the excited electrons relax back to the ground vibrational state. However, a smaller fraction may relax to either higher or lower vibrational states. As a result, light is scattered, exhibiting either elastic or inelastic behavior, which manifests as Rayleigh, Stokes, or Anti-Stokes radiation [52–54]. These distinctive types of radiation provide valuable insights into the vibrational properties of the material or molecules which serves as signatures for identifying and characterizing them. **Figure 2.10**, schematically illustrates these scattering processes.

2.4.2 Raman Scattering by Vibrational Modes in 2D TMDCs

By using a Group-Theory approach, numerous studies have analyzed the lattice modes at the $\Gamma - point$ of the Brillouin zone in the hexagonal TMDCs [55–59]. Their analysis reveals 18 vibrational modes that can be decomposed into specific irreducible representations as shown below;

$$\Gamma = 2A_{2u} + B_{2g}^{1} + B_{2g}^{2} + B_{1u} + A_{1g} + 2E_{1u} + E_{2g}^{1} + E_{2g}^{2} + E_{2u} + E_{1g} \qquad \textbf{(2.4.2)}$$

Among these, the Raman active modes are $E_{2g}^{1}, E_{2g}^{2}, E_{1g}$ and A_{1g} in 3D form. **Figure 2.11 a)** provides a schematic for these Raman active modes.

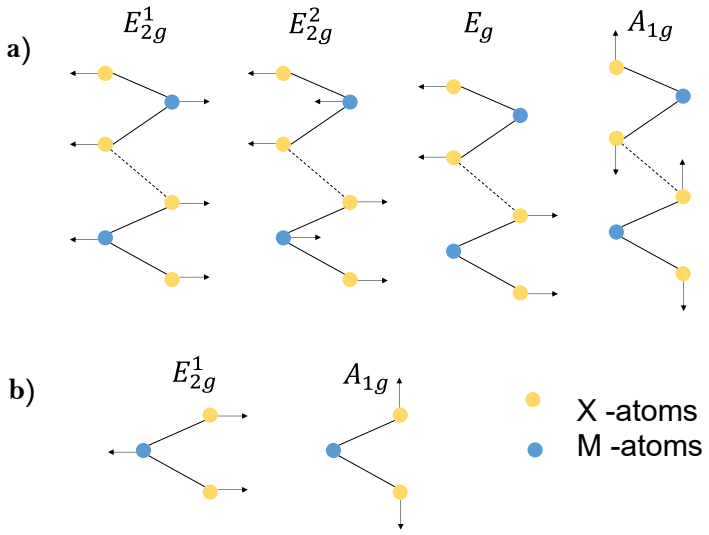

Figure 2.12: a) Schematic showing the Raman active modes in MoS_2 and WS_2. Inspired rom [55]. **b)** Schematic showing the in-plane and out-of-plane vibrational modes in monolayers of MoS_2 and WS_2.

However, in this project, we mainly analyze the in-plane (E_{2g}^{1}) and out-of-plane (A_{1g}) vibrational modes of the X-M-X layers, shown in **Figure 2.11 b)**, which are sufficient for identifying and characterizing the monolayers we fabricated. Using Raman spectroscopy, we experimentally observe the inelastically scattered light by these vibrational modes at certain frequencies relative to the

incident laser frequency and compare the data with values from literature. As will be seen further in this thesis, these two Raman-modes help us in not just characterizing the material, but also understanding the nature of their interactions with gold and other substrates.

2.5 Heterostructures of 2D TMDCs

Heterostructures, composed of stacked monolayers of different 2D materials, exhibit fascinating physics that enable various practical applications requiring efficient charge transfer and collection, such as in solar cells and photodetectors [60]. In this project, we focus on fabricating MoS_2/WS_2 heterostructures, combining MoS_2 and WS_2 monolayers. Despite lattice mismatch, the sharp edges of these monolayers, terminating with S-atoms, allow for successful stacking [60–62]. **Figure 2.12 a)** schematically illustrates the MoS_2/WS_2 heterostructure which, on being photoexcited, results in the formation of excitons, with electrons and holes localized in the MoS_2 and WS_2 monolayers, respectively.

Using DFT, the electronic band structures of these MoS_2/WS_2 heterostructures have also been calculated by different research groups [63–65]. **Figure 2.12 d)** below shows such band structures where the authors have claimed that strong interlayer coupling between the two layers enables the VBM to be located in the WS_2 monolayer, while the CBM gets located in the MoS_2 monolayer. The photoexcitation process in this heterostructure excites an electron from the $\Gamma - point$ in the VBM to the $K - point$ in the CBM of the Brillouin Zone across a staggered heterojunction [63]. This staggered heterojunctions, as depicted in **Figure 2.12 b),** further influences the evolution of excited states in these heterostructures by facilitating significant charge transfer between the layers and

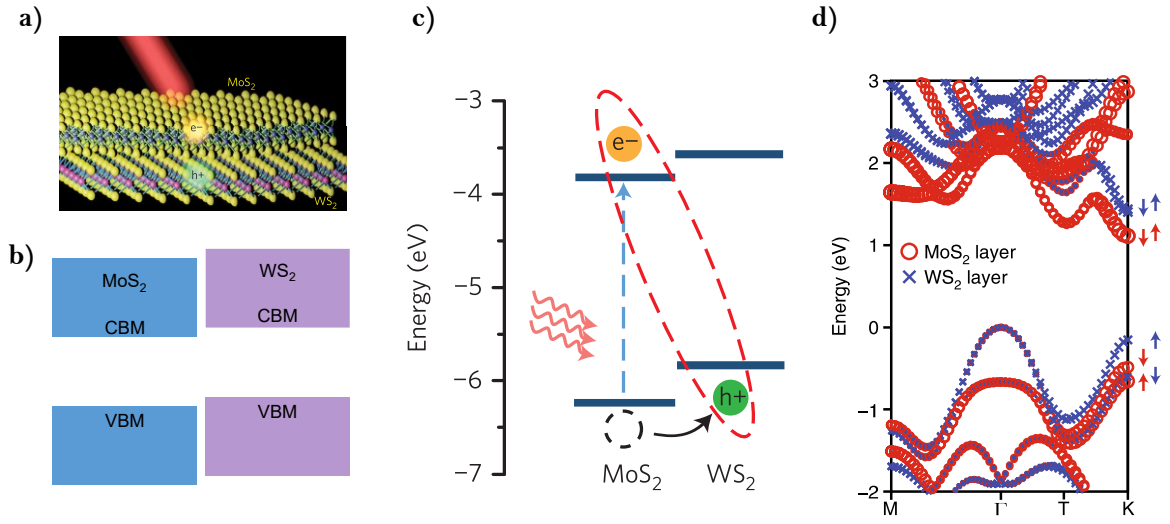

Figure: 2.13: a) Schematic for photoexcitation of MoS_2/WS_2 heterostructures leading to spatially separated electron-hole formation [67]; **b)** Schematic for staggered (Type II) band alignment in MoS_2/WS_2 heterostructures; **c)** Schematic for photoexcitation followed by charge transfer between the layers [67]; **d)** DFT calculated band structures for MoS_2/WS_2 heterostructures [63].

leading to the formation of interlayer excitons, which are Coulombically interacting electron-hole pairs separately residing in the two different materials that form the heterostructure [60,66].

Figure 2.12 c) demonstrates that photoexcited electrons in the CBM of WS_2 are transferred to the energetically lower CBM of MoS_2, while holes from the VBM of MoS_2 are transferred to the VBM of WS_2, generating interlayer excitons. This charge transfer reduces the probability of recombination between opposite charges residing in different monolayers, resulting in strong quenching of the PL spectra [67].

Apart from charge transfer, energy transfer between the individual layers is another dynamic process in these heterostructures that can affect the PL signal [66,67]. Kozawa *et al.* (2018) claimed that this energy is transferred from the material with higher bandgap to that with lower bandgap [68]. Researchers have also explored this phenomenon using hexagonal Boron Nitride (h-BN) spacer layers between MoS_2 and WS_2 monolayers, where they claimed to have observed the energy transfer processes between B-excitons in MoS_2 and A-excitons in WS_2 monolayer, which is similar to dipole-dipole interactions [69].

However, a good contact between the two monolayers leads to efficient charge transfer between them which ultimately quenches the PL from both layers. Thus, the degree of PL quenching serves as an indicator of the contact quality between the monolayers, with higher quenching suggesting a strong coupling between them [60,62,66,67].

Chapter 3

Methods

In this section, we present the methodology for obtaining large-area monolayers and analyzing their PL and Raman spectra. Our approach builds upon the methods described in previous works [32,70–74], incorporating their insights while addressing key details that were not sufficiently documented. We optimized our method for our specific needs. We fabricating an ultra-flat gold foil of around 125 nm thickness to obtain optimal contact between the gold atoms and the monolayer. Additionally, we spin-coated a 1.49 μm thick layer of PMMA on the gold foil to allow for adequate spacing between a Thermal Release Tape (TRT) and the gold foil. The purpose of this spacing was to prevent any potential roughness that could be introduced by the TRT on the gold foil and also to provide structural support to the foil. Furthermore, we used sapphire (Al_2O_3) substrates since we experimentally observed its optimal adhesion to the gold foil for transferring the monolayer to it. Whereas for other substrates such as silica, Si/SiO_2, and quartz, the adhesion was sub-optimal. To highlight the different methods we tried for fabrication and the important insights we obtained from these methods, a table is provided in **Appendix A8.** We end this chapter by shortly discussing the curve-fitting procedure to the Raman and PL spectra of the materials we studied.

3.1 Fabrication

3.1.1 Fabrication of PMMA-Coated Gold-Deposited Silicon Wafer

Gold was deposited onto a silicon wafer is through a thermal evaporation process to create a 125 nm ultra-smooth gold film. The assembly setup, as illustrated in **Figure 3.1**, involves placing the wafer on a substrate holder plate in an inverted position within the thermal evaporator. To shield the sample, a shutter plate is used. For evaporation, a tungsten boat loaded with gold serves as the source material. The current applied to the tungsten boat is gradually increased until it reaches a white-hot state and the gold starts to evaporate. The desired thickness is attained by following programmed steps and adjusting the current accordingly. Subsequently, the current is gradually decreased and eventually switched off upon reaching the desired thickness.

The next step involves spin-coating a layer of PMMA on the gold-deposited surface. PMMA 950K A8 resist from *micro resist technology GmbH* with 8% solid content in anisole is obtained for this

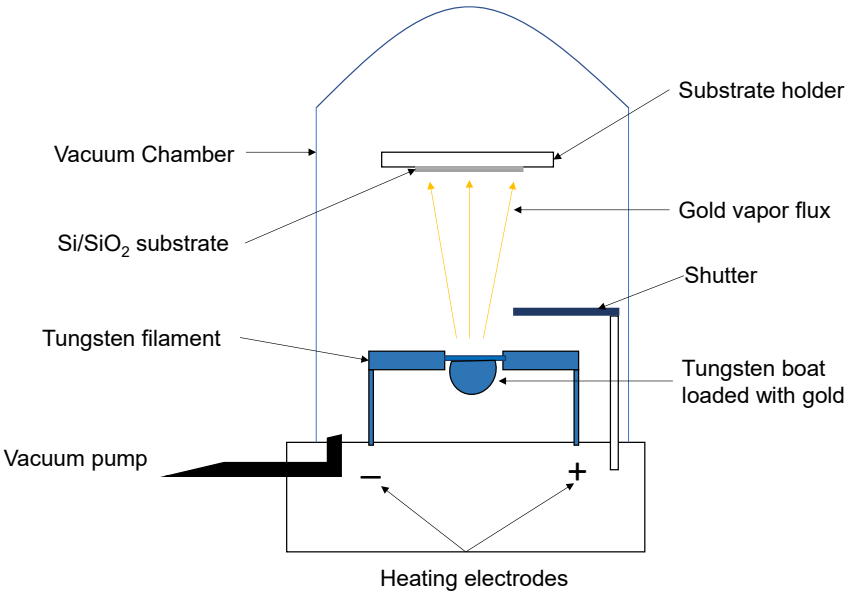

Figure 3.1: Schematic for gold-evaporation process in a vacuum chamber.

process. A preheated hot plate at 180 °C power is used to cure the PMMA. The spin-coater program is edited to include specific steps: **i)** *closing the lid within 5 seconds*; **ii)** *spinning the substrate at 2000 RPM for 60 seconds with an acceleration rate of 1000 RPM*; and **iii)** *stopping the spinning process with a deceleration rate of 1500 RPM*. To ensure adhesion, the substrate is held in place on a vacuum chuck, and wafer dicing tape is used underneath to prevent resist seepage and ensure proper vacuum.

Initially, a silicon substrate is coated with PMMA and baked at 180 °C for 90 seconds. A scratch is made on the resulting resist layer, and the height difference is measured using a profilometer. For the actual samples, the spin-coating process is repeated without the scratching and profilometer measurement. Spinning the silicon substrate at 2000 RPM results in a 1.49 μm thick resist layer.

3.1.2 Monolayer Fabrication

In this method, the necessary materials include the 2D materials for exfoliation which were purchased from *HQ Graphene*; the pre-fabricated ultra-flat gold foil coated with PMMA resist as described in the above section **3.2**; single-sided Thermal Release Tape (TRT) named *Nitto Revalpha* with a release temperature of 130 °C purchased from *Nitto*; smooth sapphire substrates with surface roughness of around 0.1-0.3 nm purchased from *Ossila*; a hot plate; acetone for dissolving PMMA; KI/I_2 or gold etchant with an etch rate of 28 angstrom/sec and density of 1.2924 g/mL at 25 °C obtained from *Sigma Aldrich*; and deionized (DI) water for removing etchant residues. **Figure 3.2** shows the entire process of fabricating the monolayer samples. The procedure begins with the application of the TRT to the PMMA-coated Au foil after it has been cut to the desired size. The *TRT-PMMA-Au* foil assembly is then detached from the Silicon wafer. Within a time frame of 5-6

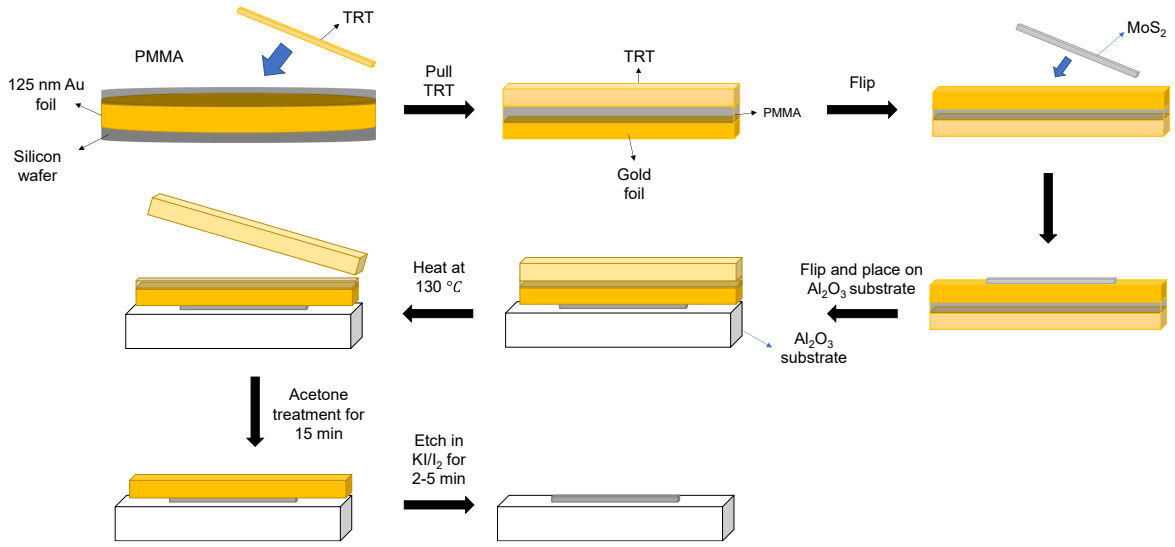

Figure 3.2: Schematic for the steps used in exfoliating the monolayers on gold and transferring them to sapphire substrates.

minutes, a transparent tape having the bulk 2D material is carefully applied to the gold foil to exfoliate the desired monolayer onto it. We further examined the material on gold using optical images and used Raman spectroscopy to confirm the presence of the monolayers based on the appearance of specific Raman modes in their Raman spectra. Then the *TRT-PMMA-Au-monolayer* assembly is gently pressed onto a smooth sapphire substrate to establish optimal contact. After heating the assembly to 130°C to remove the TRT, the PMMA layer is dissolved in acetone. Subsequently, the gold is etched using KI/I_2 etchant, followed by rinsing with DI water to remove any residual etchant, resulting in the monolayer remaining on the sapphire substrate.

3.1.3 Heterostructure Fabrication

To fabricate heterostructures involving different 2D materials, a consistent procedure is applied. Initially, a monolayer of a specific material, such as WS_2, is fabricated on a sapphire substrate

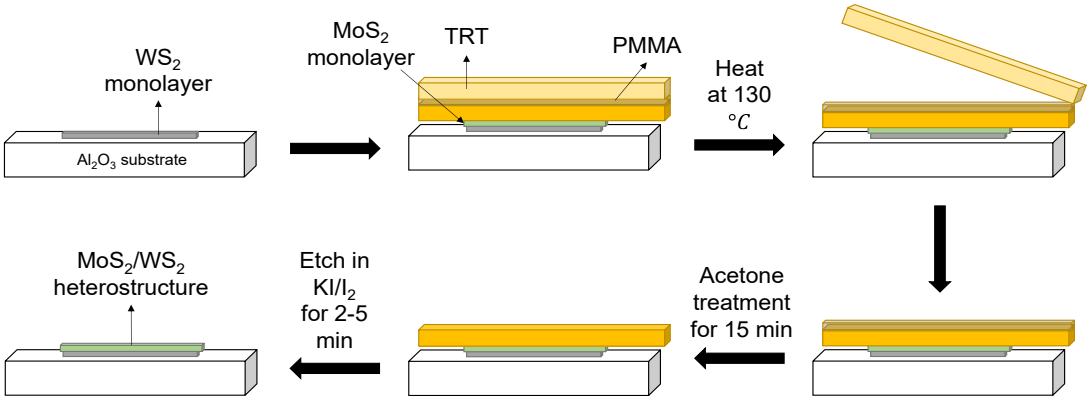

Figure 3.3: Schematic showing the fabrication of MoS_2/WS_2 heterostructure on Al_2O_3 substrate.

following the procedure outlined in section **3.1.2** above. Subsequently, another monolayer, such as MoS_2, is then exfoliated on gold. Then the MoS_2 monolayer on gold is carefully positioned on top of the WS_2 monolayer to create the desired heterostructure configuration.

Next, the *TRT-PMMA-Au-MoS_2-WS_2-Al_2O_3* configuration is subjected to a heating process at 130°C to facilitate the removal of the TRT, as depicted in **Figure 3.3**. Subsequently, using the same methodology as described in section **3.1.2**, the configuration undergoes a series of steps involving acetone treatment for PMMA removal, followed by gold etching and rinsing with DI water. These procedures result in the MoS_2/WS_2 heterostructure being firmly established on the sapphire substrate, forming the desired heterostructure configuration.

3.2 Monolayer Analysis

After exfoliating the material on gold, we took optical images to identify regions on the gold foil potentially containing monolayers. To confirm the presence of monolayers, we used Raman spectroscopy, and after etching the gold, we compared the Raman spectra of different layer numbers with values reported in the literature. Moreover, compared the Raman and PL spectra of these monolayers on gold with those not bound to gold, which we obtained by etching of the gold using KI/I_2 etchant. This approach enabled us to gain some valuable insights into the characteristic differences between the vibrational and optoelectronic properties of the monolayers on and off gold substrates.

3.3 Spectroscopy Methods

For the characterization and evaluation of our monolayer samples, Raman and PL spectroscopy were performed using the *WITec Alpha300* confocal Raman microscope. **Figure 3.4** illustrates the schematic of the experimental setup employed.

In this setup, an LED lamp illuminates the monolayer sample, which is placed on a motorized Piezo stage. The reflected light from the sample is directed by a beam-splitter (BS) into the camera, generating an optical image. Both Raman and PL spectroscopy are conducted using a continuous wave (CW) laser with a wavelength of 532 nm. To focus the laser beam onto specific spots in the sample, a 100x objective with a numerical aperture of 0.9 is used. The spectrometer captures the scattered Raman and PL signals from the sample, which passes through the same 100x objective. However, different gratings are used in the spectrometer for Raman and PL detection. Specifically, a grating with 1,800 grooves per mm is used for Raman spectroscopy, while a grating with 150 grooves per mm is employed for PL spectroscopy.

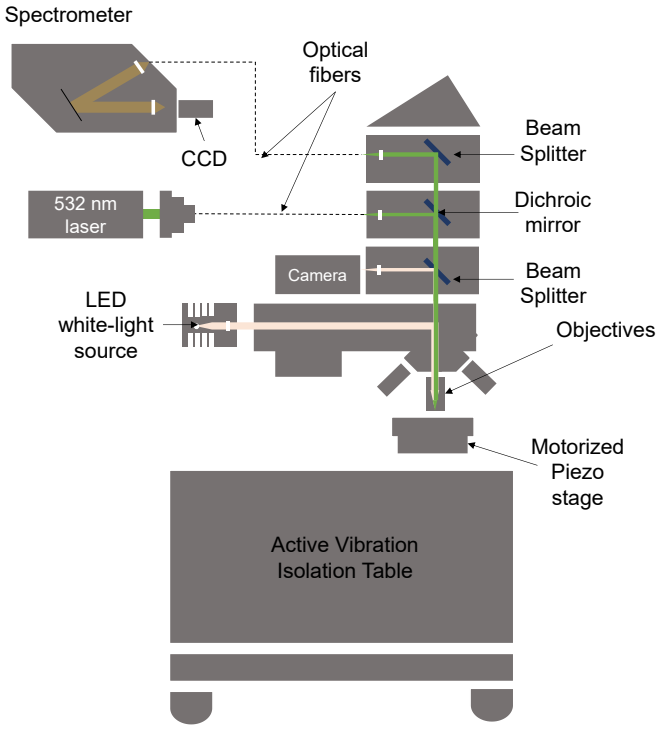

Figure 3.4: Schematic of the *WITec Alpha300* confocal microscope used for Raman and PL spectroscopy.

Using this setup, we acquired Raman and PL maps over specific areas of the sample. The dimensions of the scanned maps were 40 $\mu m \times 40\ \mu m$, with 100 lines per map and 100 pixels per line, resulting in a total of 10,000 pixels over an area of 1,600 μm^2 of the sample. This scanning configuration provided us with a high resolution for detailed analysis and characterization of the monolayer samples.

3.4 Lorentz Function Fitting

To analyze the optoelectronic and vibrational properties of the TMDC monolayers, we fit Lorentz functions to their PL and Raman spectra. The Lorentz function is commonly used for fitting spectral line-shapes associated with resonant processes, such as electronic transitions in these materials. This enables us to obtain valuable information about the underlying optoelectronic properties of the materials, which helps us to assess their quality. The Lorentz function is given by the equation **(3.4.1)** [75]

$$f(x, x_0, \gamma) = \frac{1}{\pi\gamma\left[1 + \left(\frac{x - x_0}{\gamma}\right)^2\right]} . \qquad \textbf{(3.4.1)}$$

This function is fitted to the data to extract two important parameters, the peak position x_0, and the half-width at half-maximum (HWHM), γ, as shown in **Figure 3.5 a).** The full-width at half-maximum (FWHM) can be calculated as twice of HWHM.

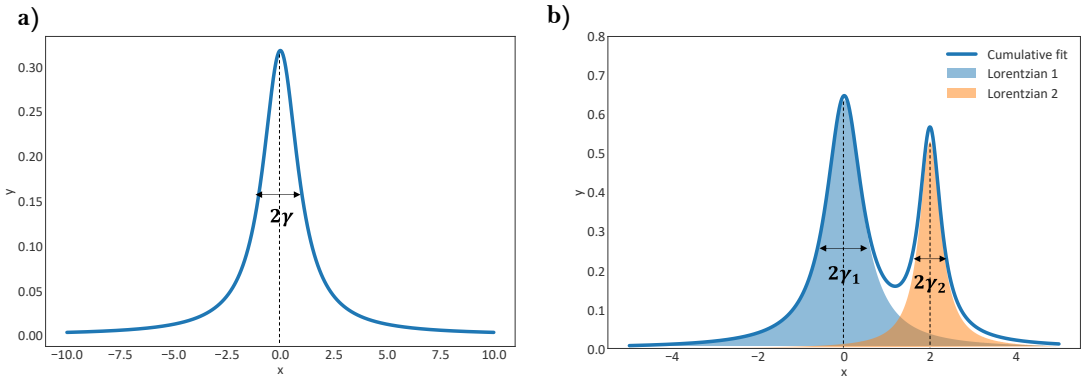

Figure 3.5: a) Lorentzian plot with parameters x_0 (peak position) and γ (HWHM); **b)** Two Lorentz functions with individual set of parameters contributing to a cumulative fit.

However, in our project, we modify this function to account for background noise (y_0), and the area under the curve (a). By examining the location and number of the peaks in the spectrum, we can fit the data with this function. **Figure 3.5 b)** illustrates an example of a two-peak spectrum and how the parameters are incorporated into the modified Lorentz function. The extracted parameters from the fit $(a_1, x_1, \gamma_1, a_2, x_2, \gamma_2)$ are included in the modified Lorentz function as shown below

$$f(x, y_0, a_1, x_1, \gamma_1, a_2, x_2, \gamma_2) = y_0 + a_1\left(\frac{1}{\pi\gamma_1\left[1+\left(\frac{x-x_1}{\gamma_1}\right)^2\right]}\right) + a_2\left(\frac{1}{\pi\gamma_2\left[1+\left(\frac{x-x_2}{\gamma_2}\right)^2\right]}\right) \quad \textbf{(3.4.2)}$$

In **Figure 3.5 b)**, the background is at $y_0 = 0$, and the shaded blue and orange areas represent the areas under the two Lorentz curves. The HWHMs of the Lorentzian functions are denoted by γ_1 and γ_2. By fitting the data with this modified Lorentz function, we can obtain reliable values for the peak positions, widths and the integrated intensities for Raman and PL spectra.

Chapter 4

Results and Discussions

4.1 Material and its Properties On and Off Gold

4.1.1 Large Monolayers Exfoliated on Gold Foil

Optical microscopy images of MoS_2 and WS_2 on gold shown in **Figure 4.1 (a & b)** were subsequently analyzed for monolayer identification using color contrast (shown on the right). The monolayer coverage area for MoS_2 and WS_2 on gold were roughly around $\mathbf{2.5}\ \boldsymbol{mm} \times \mathbf{2}\ \boldsymbol{mm}$ and $\mathbf{0.5}\ \boldsymbol{mm} \times \mathbf{1.5}\ \boldsymbol{mm}$ respectively. There are multiple breaks in the monolayer coverage, which is most likely due to structural defects in the lattice, contamination of the gold surface, and/or mechanical stress during the exfoliation process. Furthermore, discontinuities in the bulk crystal from which the monolayers are exfoliated is another highly probable reason for these breaks. Nevertheless, the images indicate good crystal uniformity of the monolayers over appreciable areas.

The higher number of observable bulk pieces in WS_2 on gold compared to MoS_2 can be due to two factors. Firstly, the use of normal transparent tape during exfoliation may have resulted in a higher yield of bulk pieces for WS_2 compared to the use of normal scotch tape for MoS_2 exfoliation owing to its comparatively higher adhesion. Residues from the transparent tape are visibly present at multiple positions, providing evidence of the tape's involvement in the exfoliation process. However, the transparent tape proved to be more effective as compared to normal scotch tape in the subsequent trials for exfoliating large monolayers of both MoS_2 and WS_2, owing again to its higher adhesion.

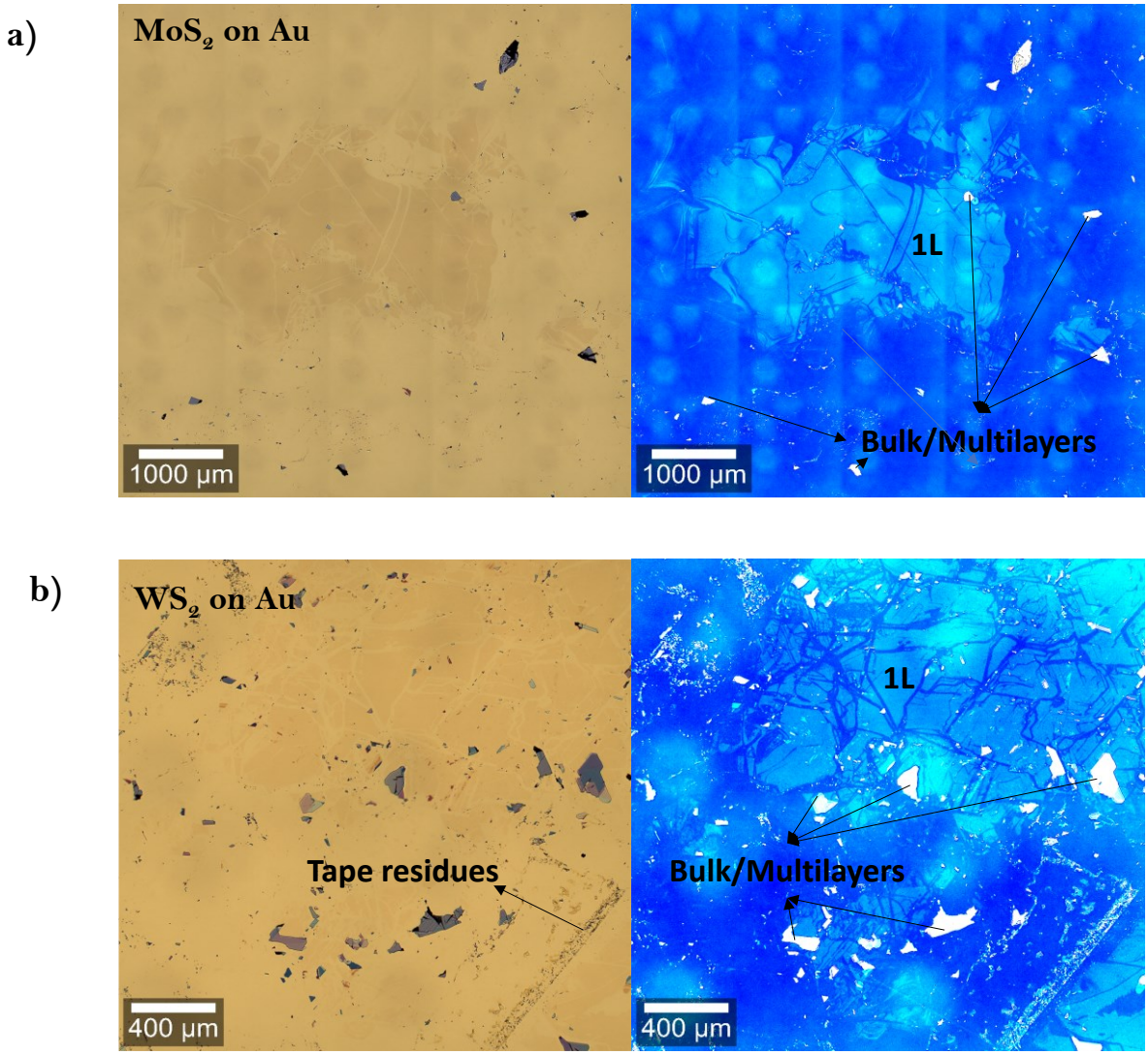

Figure 4.1 a), b): (*Left*) Optical microscopic images for MoS_2 and WS_2 on gold. (*Right*) Blue filling to observe color contrast between monolayer, gold and multilayers.

Secondly, the slightly extended exposure of the WS_2 sample to air for nearly six minutes before exfoliation could have led to the deposition of contaminants on the gold surface, exacerbating the contact between the monolayer and the topmost gold layer, and resulting in a lower yield of monolayers [13].

4.1.2 Raman Spectra

4.1.2.1 MoS_2

We use Raman spectroscopy to identify the number of layers of a sample. Bright field images of a characteristics investigated sample are shown in **Figure 4.2** before and after etching of the gold .By comparing our data with previous literature, we verify the presence of monolayers and confirm the identification of subsequent few layers. Additionally, we investigate the distinct vibrational properties of MoS_2 before and after the removal of the gold substrate and observe the impact of the gold on the material's vibrational behavior.

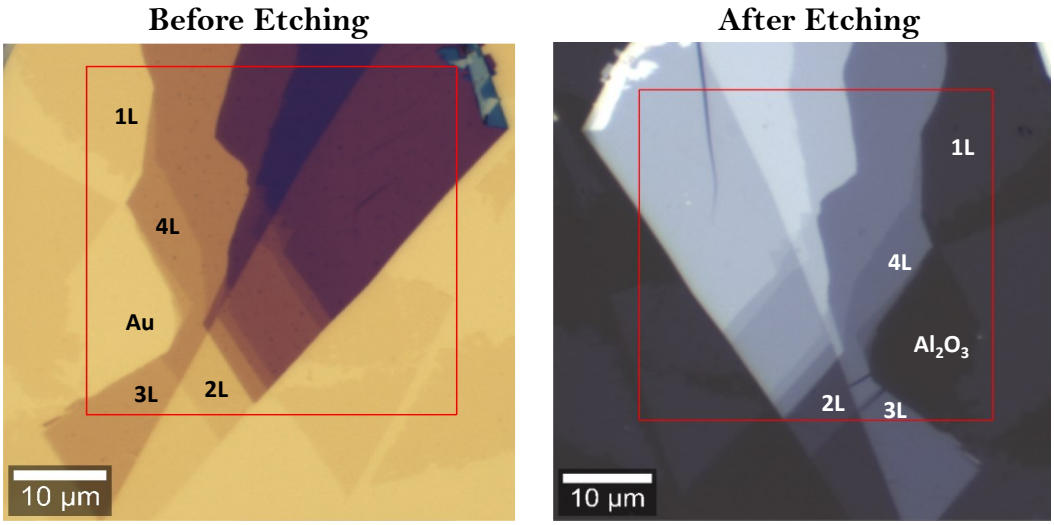

Figure 4.2: Different MoS_2 layer numbers before etching on Au (*left*) , and after etching on Al_2O_3 substrate (*right*). Red squares refer to regions for which the maps were obtained.

The layer sequence before gold etching was *MoS_2 (1L and multilayers) – Au – PMMA – TRT*, while after etching it becomes *MoS_2 (1L and multilayers) – Al_2O_3 substrate*. The change in the dielectric environment surrounding the MoS_2 layers before and after etching results in a noticeable difference in color between the two images. To compare the Raman spectra, measurements were taken at nearly identical positions on the MoS_2 layers before and after etching.

Corresponding Raman spectra are shown in **Figure 4.3** Each layer exhibits distinct peaks corresponding to the in-plane vibration or the E^1_{2g} mode (*left peak*) and the out-of-plane vibration or the A_{1g} mode (*right peak*. The frequencies of these vibrational modes vary depending on the layer number. To verify the layer numbers, we compared our Raman spectra data of MoS_2 layers off gold with the results reported by Li *et al. (2012)* (**Figure 4.3 b)**) [76]. Good agreement is observed. The minor differences can be attributed to difference in the substrates used, with Li *et al.* using Si/SiO_2 substrate and our study using Al_2O_3 substrate.

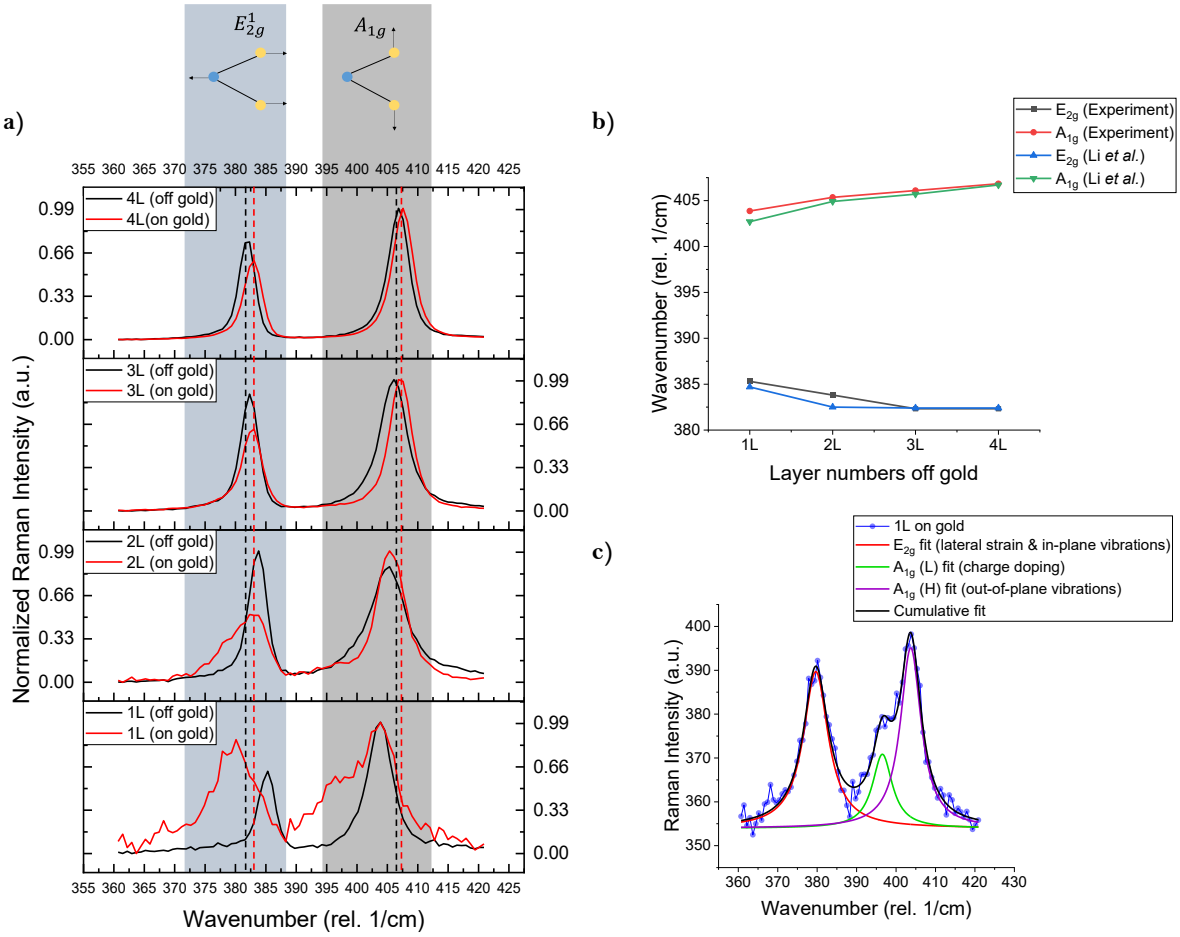

Figure 4.3: a) Stacked plots of Raman spectra for different layer numbers on and off gold. Red dotted lines indicate the E_{2g} and A_{1g} peak frequencies for $4L$ MoS_2 on Au, whereas black dotted lines represent the same quantities for $4L$ MoS_2 off Au; **b)** Comparison of Raman peak values for different layer numbers with Li *et al.'s* values; **c)** Raman spectra for MoS_2 monolayer on gold where three Lorentz functions are fitted.

Notable differences, however, are observed in the Raman spectra of the first two layers of MoS_2 on and off gold. Specifically, the in-plane vibrations or the E^1_{2g} mode exhibit suppression or red-shifted frequencies, along with increased FWHM. This effect is particularly pronounced in the first layer of MoS_2 in contact with the gold foil. This has been associated with strong covalent-like quasi bonding (CLQB) interactions between the Au-atoms and the lowermost layer of S-atoms of MoS_2 [30,31]. Additionally, the increased FWHM of the E_{2g} mode is indicative of heterogeneous biaxial strain on the MoS_2 layers, resulting from the lattice mismatch between MoS_2 and the underlying gold layer [77].

Furthermore, the MoS_2 monolayer on gold shows a lower-frequency shoulder appearing at around 396 *rel. 1/cm*. This has been attributed to another underlying Raman mode $A_{1g}(L)$ in addition to the out-of-plane vibration mode at around 405 *rel. 1/cm*. This lower frequency mode is related to the charge transfer or doping from the monolayer to the gold[77]. By fitting Lorentz functions to the this part of the spectrum, we can discern the contributions of the in-plane and out-of-plane vibrations, and also of strain and charge doping to the Raman spectra of the monolayers on gold as shown in

Figure 4.3 c). Specifically, the E_{2g}^1 mode provides insight into the level of in-plane-vibrations and lateral strain on the monolayer. The $A_{1g}(L)$ corresponds to the degree of charge doping or charge transfer to the gold, and $A_{1g}(H)$ represents the out-of-plane vibrations. Notably, charge transfer to the gold substrate leads to quenching of the PL spectrum of the monolayer on gold, a topic discussed in detail in Section **4.1.3**, where we compare the PL spectra of the monolayer on and off gold.

4.1.2.2 WS_2

Interestingly, for WS_2, we observe many more underlying Raman modes for all the layers. Importantly, we observe that the E_{2g}^1 mode is red-shifted for the WS_2 monolayer on gold (**Figure 4.4 c)**). Following from our previous discussion on MoS_2, we speculate that this is also due to the suppression of the in-plane vibrations in the monolayer due to strong CLQB interactions with the gold layer. We also observe that this red-shift of the in-plane vibrational modes is only for the monolayer on gold, while for the other layers both on and off gold, they are almost at same frequencies .(**Figure 4.4 a)**).

We also observe the splitting of the A_{1g} mode of the monolayer on gold into two modes. Since to the best of our knowledge, we could not find any literature on Raman modes for WS_2 on gold, we speculate that this splitting is also due to charge doping experienced by the monolayer, similar to the MoS_2 monolayer. Thus, for WS_2 monolayers also, we observe the quenching of the PL spectra due to this charge transfer from the monolayer to the gold **(Appendix A4)**. In order to confirm our assigned layer numbers, we cross-validated our data with values from literature. We compared the Raman frequencies with Qiao *et al.* 's values and found that they closely match [78]. Here, we compare the values for only three layers due to unavailability of data from literature for the fourth layer. We also observe a higher FWHM of the E_{2g}^1 mode for the WS_2 monolayer both on and off the gold, and following from our previous discussion on MoS_2, we speculate this to be due to an increased level of strain experienced by the monolayer due to lattice mismatch with both the gold and the sapphire substrate.

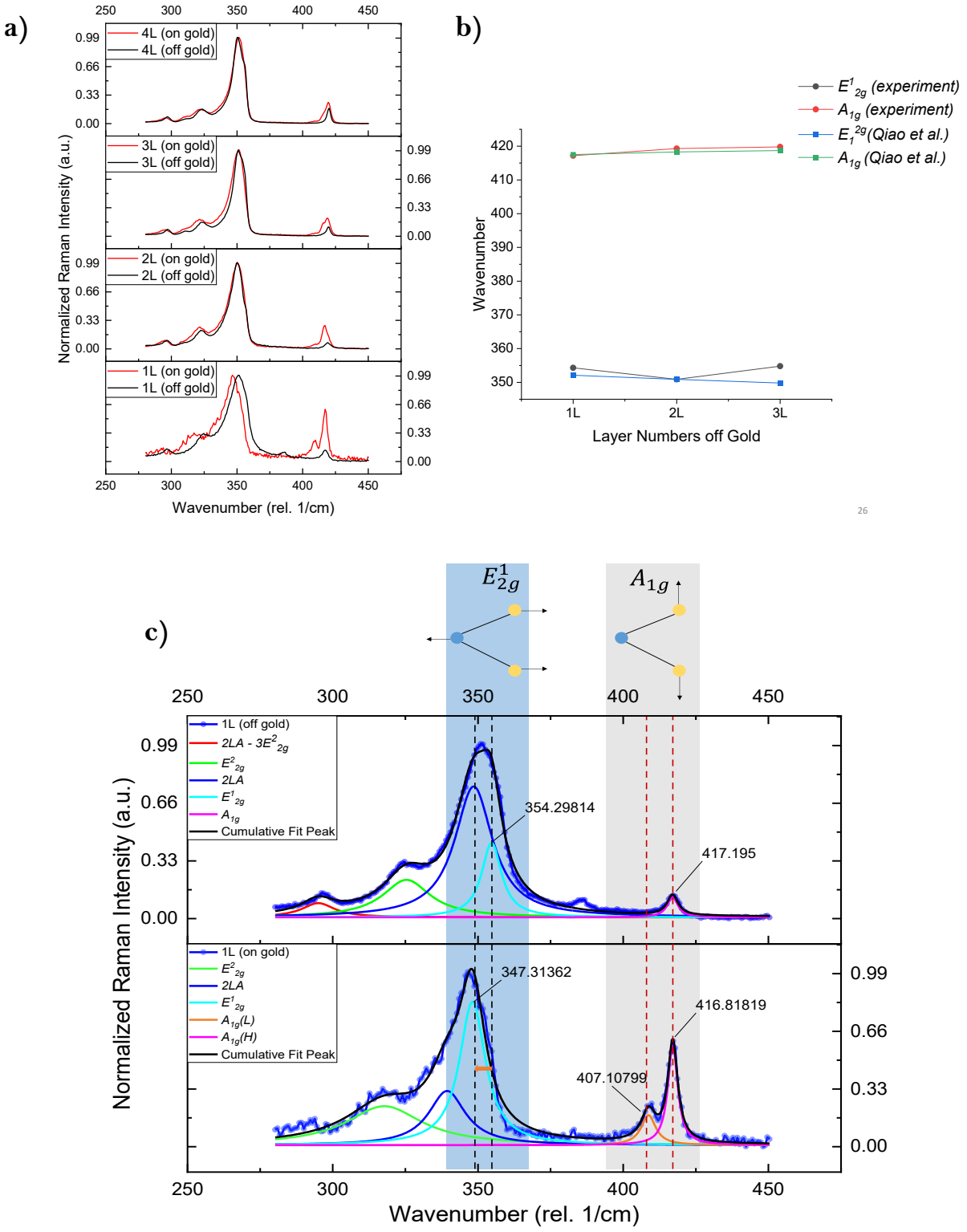

Figure 4.4: **a)** Raman spectra of different numbers of WS_2 layers, both on and off gold; **b)** Comparison of the Raman frequencies of the E^1_{2g} and A_{1g} modes with values from literature; **c)** Lorentz functions fitted to the Raman spectra of WS_2 monolayer on and off gold. Black dotted lines indicate position of E^1_{2g} mode for WS_2 monolayer on (*below*) and off *(above)* the gold. Red dotter lines indicate the splitting of the A_{1g} mode into two, with the lower frequency mode at 407.1 rel. 1/cm representing charge doping from monolayer to Au.

4.1.2.3 Summary of the Analysis of Raman Spectra

In summary, the analysis of the Raman spectra for different layers of MoS_2 and WS_2 provided valuable insights into their vibrational properties. We confirmed the presence of monolayers and subsequent few layers, and compared with literature data to validate the layer numbers. The presence of a gold layer resulted in red-shifted frequencies for both materials, indicating strong CLQB interactions. Increased FWHM values indicated higher strain experienced by the monolayers due to lattice mismatch with the gold layer. The splitting of the A_{1g} peak and PL quenching in both MoS_2 and WS_2 monolayers were attributed to charge doping which was coherent with our observations for quenched PL in the monolayers. These findings highlight the influence of gold and provide insights into the vibrational properties of MoS_2 and WS_2 samples on and off the gold foil.

4.1.3 Quenched Photoluminescence on Gold foil

The PL spectra, plotted in **Figure 4.5 b),** shows peaks at around $E = 1.83\ eV$ and $E = 2.1\ eV$, characteristic for A-exciton and B-exciton in MoS_2 respectively. However, we noted a significant quenching of the PL spectra of both MoS_2 and WS_2 monolayers upon contact with gold. This is illustrated in **Figure 4.5 a)** which shows PL maps for MoS_2 before and after etching the gold layer. Interestingly, after the gold is etched, the PL signal reappears. We observed that after the gold is etched, the PL signal from the monolayer is much stronger than PL from the other layer numbers. This is mainly because the monolayer has a direct bandgap while other layers have indirect bandgap as discussed in section **2.1.**

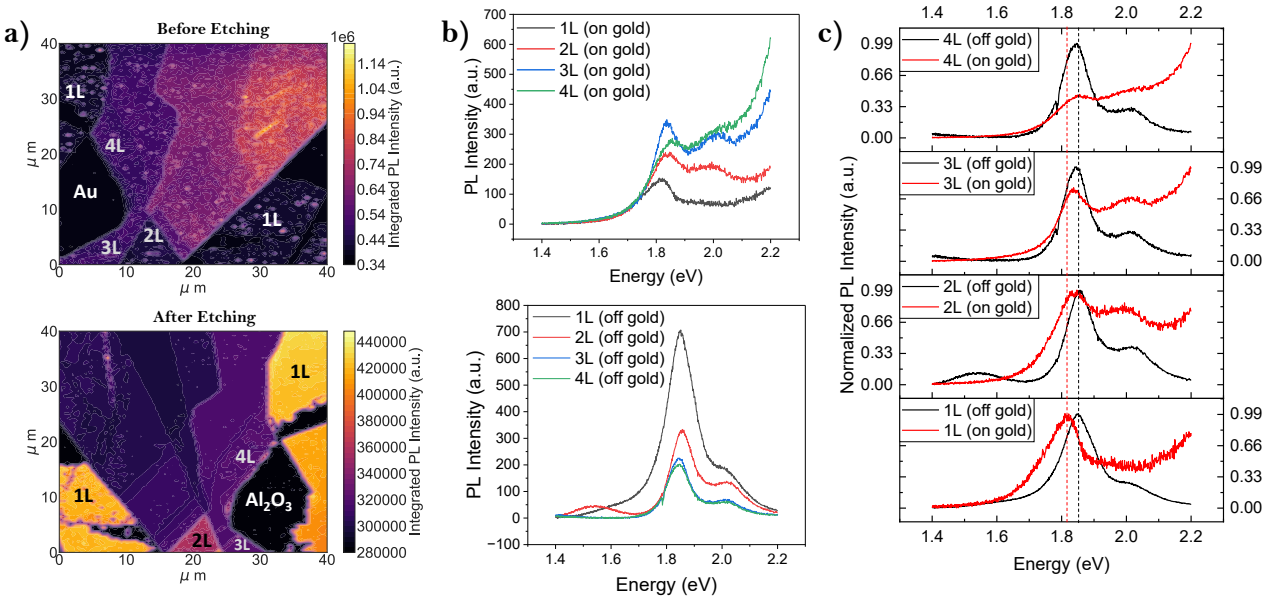

Figure 4.5: a) PL intensity maps for MoS_2 layers on (*above*) and off (*below*) gold; **b)** Comparison of PL signals for different layer numbers on (*above*) and off (*below*) gold; **c)** Stacked plot of normalized PL spectra for different layer numbers on and off gold.

The presence of gold introduces a difference in the work-functions between the gold layer (~5.1 eV) and the semiconducting MoS_2 monolayer (~4.7 eV) in contact with it. This difference leads to the formation of a Schottky barrier height of approximately 0.3 eV, as the Fermi levels of the two materials tend to align upon contact [77] (**Appendix A2).** Consequently, electrons from the conduction band of the MoS_2 monolayer diffuse into the gold layer until the Schottky-barrier height is established leading to bending of the bands at the interface [77]. This charge transfer mechanism depletes the monolayer of electrons available for radiative recombination with holes in its valence band, leading to the observed quenching of the PL. The similar work-function values for WS_2 and MoS_2 explains the quenching effect observed in WS_2 monolayers as well [79].

The presence of faded pink spots in **Figure 4.5 a)**, representing the appearance of PL signals at certain positions of the monolayer on gold, suggests that not all areas of the monolayer are in direct

contact with the gold foil. In these regions, where intimate contact between the gold and monolayer is lacking, charge transfer from the monolayer to the gold is minimal to none, allowing for PL signals to be observed. In contrast, when the monolayer is in contact with the gold foil, the PL is significantly quenched. A similar observation of these spots can also be seen on the multilayers, likely indicating the absence of consecutive layers at those specific positions within the multilayer stack.

Furthermore, the PL spectra in **Figure 4.5 c)** shows that the A-exciton PL peak for MoS_2 monolayer on gold is slightly red-shifted by around 0.02 eV. We speculate that this is due to strain arising out of lattice mismatch between the MoS_2 layers and the gold layer. Another possibility is the formation of charged excitonic complexes such as trions, which could be formed after the excitons are photoexcited and they start to interact Coulombically with the free electrons in gold.

Similar observations are made for WS_2, which we provide in **Appendix A4.**

4.2 Quality Comparison

In this section, we present a comparative analysis of the quality of our samples in relation to those obtained through chemical vapor deposition (CVD) and mechanical exfoliation. The latter flakes were further transferred to a sapphire substrate via polydimethylsiloxane (PDMS) transfer method. To assess the quality, we fit the PL spectra of all three monolayer samples of MoS_2 and WS_2. Depending on the material, we employ one or two Lorentz functions to model the PL spectra. For WS_2 samples, we exclude the contribution of the B-exciton. This decision is based on the significantly higher energy of the PL peak associated with the B-exciton, which arises from the larger splitting of the valence band in WS_2, thereby making it difficult to observe in our *WITec Alpha300* set-up.

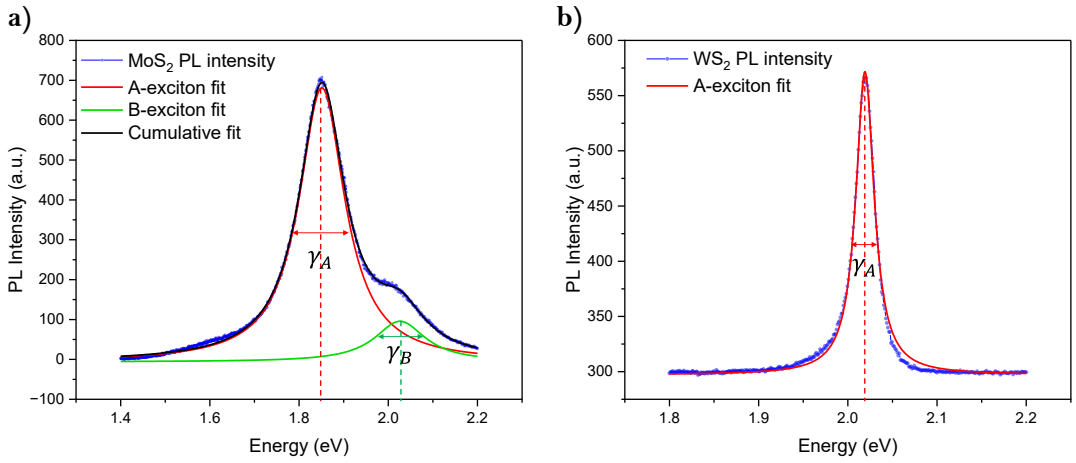

Figure 4.6: Fitted Lorentz curves to the PL spectra for **a)** MoS_2 monolayer; and **b)** WS_2 monolayer

Examples of fitted PL curves of the MoS_2 and WS_2 monolayer samples are shown in **Figure 4.6 a)** and **b**. From the fit, we extract three important parameters and their distribution to analyze the quality of our samples: **i)** *the peak energy positions of the A- and B-excitons (denoted by the vertical dotted lines)*; **ii)** *the FWHM of these peaks (γ_A and γ_B)*; and **iii)** *the integrated number of photons emitted (area under the fitted curves)*. By performing this fit for each PL spectrum obtained for each pixel of the image, we obtain a distribution of the parameters that allows the assessment of the quality of the samples.

Through the analysis of these three parameters for the three samples of MoS_2 and WS_2, we can gain valuable insights into the extent of disorder, defects, and strain within them. For instance, the FWHM value is indicative of disorder and the amount of non-radiative decay pathways as discussed in section **2.2.4.** In the case of localized excitons and also excitons scattered to different momenta due to exciton-phonon scattering processes, the PL linewidth increases [80,81]. Another parameter of interest is the occurrence of red-shifted A-exciton peaks, which provides information about the level of in-plane tensile strain in the material [82].

In the case of MoS_2, another parameter that offers insights into defect density is the ratio between the integrated PL intensities of B-excitons and A-excitons [83]. In a defect-free sample, the presence of an additional relaxation channel for B-excitons to relax to A-excitonic states significantly increases the population of the A-excitons. This results in a significantly higher PL intensity for A-excitons. However, the presence of defects leads to higher non-radiative recombination rates, thereby reducing the A-exciton PL intensity while the intensity of B-excitons remains relatively unchanged. As a result, the B/A intensity ratio changes accordingly [81]. A higher B/A ratio indicates a higher defect density within the material.

4.2.1 Quality Comparison for MoS_2 Monolayer

Bright-field images of the three samples we compared are shown in **Figure 4.7**: sample fabricated using **a)** Chemical Vapor Deposition (CVD) method; **b)** Gold-assisted exfoliation (GAE) method;

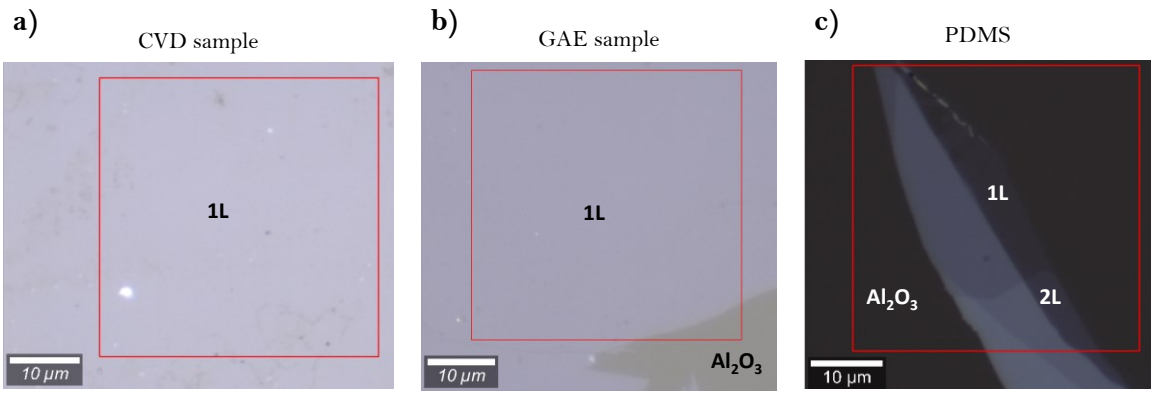

Figure 4.7: The three different MoS_2 samples used for quality comparison. Red squares are patches for which the PL maps were taken. These maps are shown in **Appendix 5** .

and **c)** Mechanical exfoliation using PDMS transfer method. Both CVD and GAE samples are large-area monolayer samples, whereas the PDMS sample has the monolayer only over an extremely small patch.

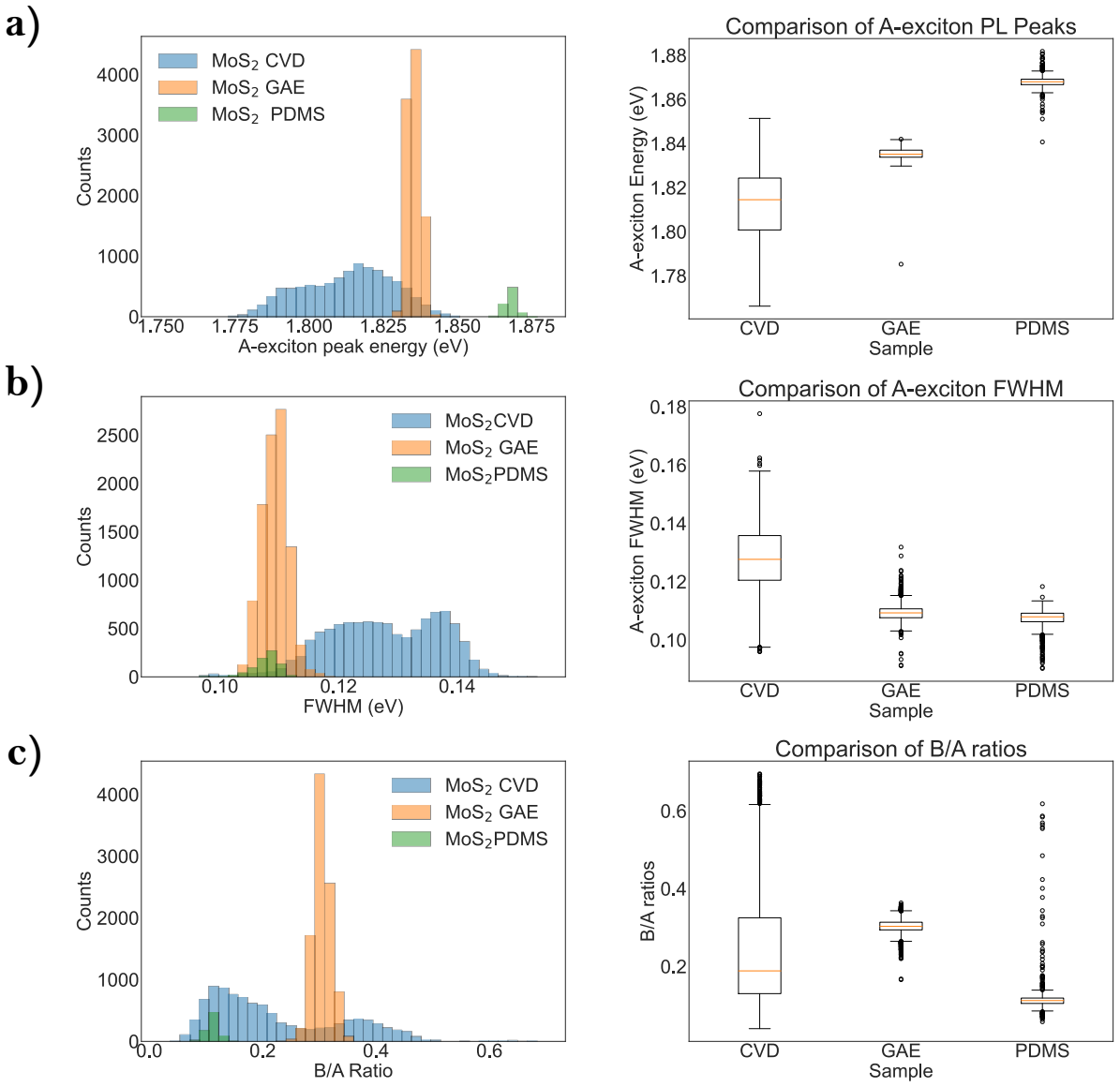

Figure 4.8: Box-plots (*left*) and histogram plots (*right*) showing the distribution the extracted parameters in the three samples. **a)** Distribution of the A-exciton peak energies; **b)** distribution of the A-exciton FWHM; **c)** distribution of the B/A intensity ratios. Maps for the three parameters for all three samples are provided in the **Appendix A5.**

Figure 4.8 shows the distribution of the three parameters extracted from the pixel-by-pixel PL spectra for the MoS_2. Comparing the A-exciton energies, the CVD sample exhibits a significant red-shift in comparison to both the GAE and PDMS samples. This observation suggests a higher occurrence of strain in the CVD sample, with a bimodal distribution indicating the presence of two distinct populations experiencing varying levels of strain. In contrast, the GAE samples display lower red-shifts and narrower distributions, indicating lower and more uniformly distributed strain.

We speculate that this uniform strain in the GAE sample may have been introduced during a chemical treatment, such as etching. Notably, the PDMS sample shows a median population with energy around 1.87 eV, closely resembling the A-exciton peak energy of a pristine MoS_2 monolayer, indicating minimal strain in this sample.

The higher FWHM value observed in the CVD sample, compared to both the GAE and PDMS samples, suggests a higher occurrence of non-radiative recombinations in the CVD sample. Interestingly, the bimodal distribution of FWHM in the CVD sample again indicates the presence of two distinct populations. The underlying reasons for this phenomenon are not yet fully understood; however, we speculate that these populations decay through different recombination pathways. In contrast, the GAE and PDMS samples exhibit similar median FWHM values. Furthermore, the narrower distribution of FWHM in the GAE sample implies relatively consistent decay dynamics across different positions in them.

Contrary to expectations, the B/A intensity ratios reveal that around 75% of the population of positions in the CVD sample have lower defect densities compared to the GAE sample. Although we are unsure about the origin of this observation, we attribute this to certain localized positions within the CVD sample exhibiting appreciably better emissive properties than the GAE sample, with almost half of the total positions in the map, while globally around 25% of the total population in the sample are positions with other structural defects ranging from sulfur vacancies to grain boundaries which lead to even higher non-radiative recombination events. This might pose a challenge in applications that require charge separation and collection. Few noticeable outliers for high B/A ratio in the PDMS sample is related to the regions in the monolayer which is twisted on the edges. This is evident from the B/A ratio map for PDMS sample provided in the **Appendix A5.**

In summary, our analysis leads us to the conclusion that our GAE samples exhibit higher quality compared to commercially prepared CVD samples of MoS_2. This conclusion is based on the lower occurrence of non-radiative recombinations and strain globally, as observed in the GAE sample. Although the PDMS sample demonstrates superior qualities among the three, its practical application is limited by its extremely small size. Furthermore, our findings indicate the presence of two distinct populations within the CVD sample, each exhibiting different emissive properties probably due to different recombination pathways within the same sample. The distribution of B/A intensity ratios suggests that a subset of the CVD sample population displays higher and more favorable emissive properties than the GAE sample. We speculate this phenomenon to be due to certain localized areas within the CVD sample having low defect densities. However, the overall presence of other defects in the CVD sample leads to significantly higher non-radiative recombinations, making it unpredictable and impractical for large scale applications.

4.2.2 Quality Comparison for WS_2 Monolayer

Our analysis of WS_2 samples revealed similar findings, as depicted in **Figure 4.9**. Both the A-exciton peak position and the FWHM measurements indicate that the CVD samples exhibit lower quality compared to the GAE and PDMS samples. **Figure 4.9 a)** illustrates that the median value for A-exciton peak energy of the CVD sample is significantly red-shifted compared to the GAE and PDMS samples, indicating comparatively higher level of strain in the monolayer of the CVD sample. Interestingly, the GAE sample displays a median value much closer to that of the PDMS sample, with a highly narrow distribution. This suggests that the quality of the GAE sample closely resembles that of a pristine WS_2 monolayer.

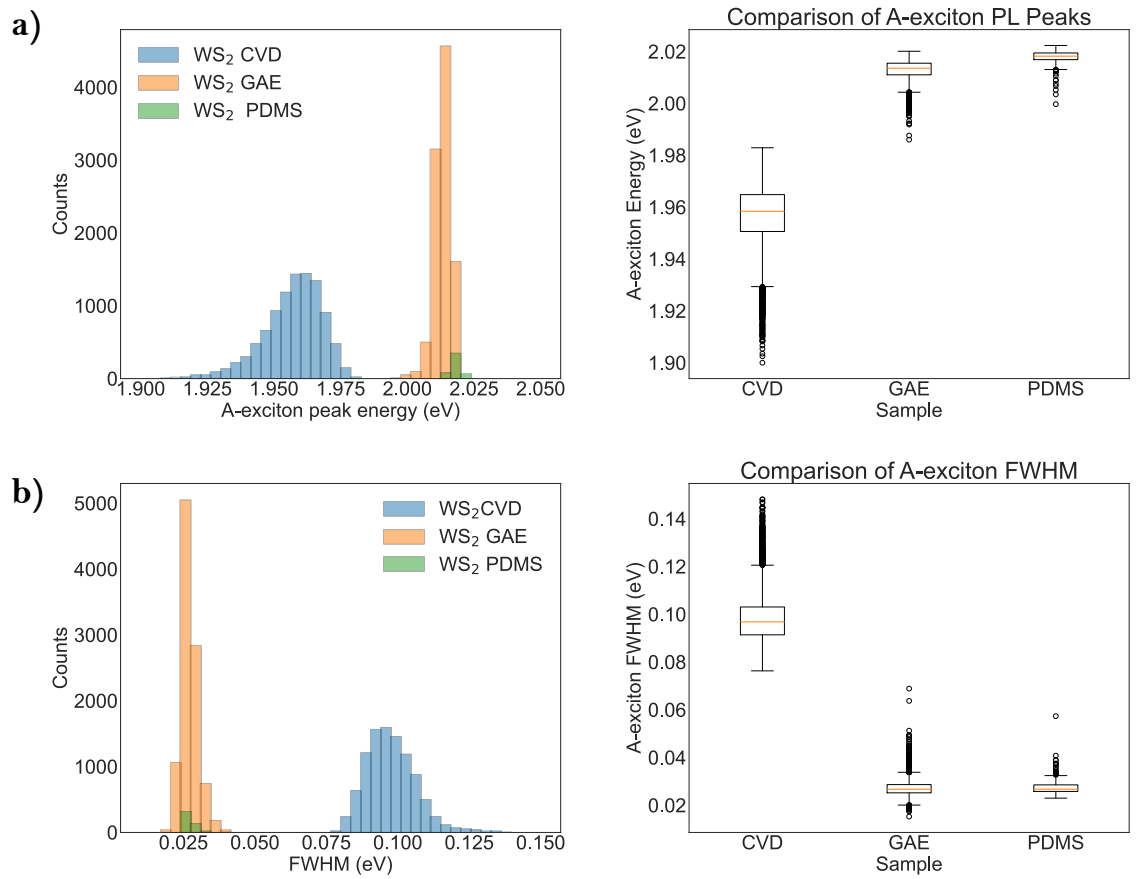

Figure 4.9: Histogram plots (*left*) and box-plots (*right*) showing the distribution the extracted parameters in the three WS_2 samples. **a)** Distribution of the A-exciton peak energies; **b)** distribution of the A-exciton FWHM

Furthermore, it is important to note that the CVD sample of WS_2 exhibits a higher variance in the distribution of red-shifted peaks compared to the GAE and PDMS samples. However, unlike the CVD sample of MoS_2, we do not observe a bimodal distribution in the WS_2 CVD sample. This suggests that the strain distribution within the WS_2 CVD sample is more uniform and does not exhibit distinct subpopulations with significantly different levels of strain.

Moreover, the FWHM distribution in **Figure 4.9 b)** provides additional evidence of lower disorder and defects in the GAE sample compared to the CVD sample. The narrower distribution of the GAE sample indicates a higher level of uniformity in terms of emissive properties, suggesting a more consistent and reliable performance for large-scale applications. This further supports the conclusion that the GAE sample exhibits superior quality and lower non-radiative recombination pathways compared to the CVD sample.

4.2.3 Summary of Analysis for Quality Comparison

The analysis of MoS_2 and WS_2 samples obtained through chemical vapor deposition (CVD), gold-assisted exfoliation (GAE), and polydimethylsiloxane (PDMS) transfer techniques provided valuable insights into their quality and characteristics. The GAE samples exhibited median values for distributions of A-exciton peak position and FWHM that were closer to pristine monolayers, suggesting higher quality and lower disorder as compared to CVD samples. In the case of WS_2, we observed that the quality of the GAE samples is extremely close to that of the PDMS sample and with monolayer sizes roughly four times the size of PDMS for the same mapping area. These observations indicate the effectivity of the GAE method in retaining the quality while also allowing for the successful exfoliation of large-area monolayers.

4.3 Heterostructure Samples

4.3.1 Optical Images of Fabricated Heterostructures

Using the methods outlined in section ***3.2.3***, we attempted to fabricate the MoS_2/WS_2 heterostructures. We fabricated two heterostructures with one having MoS_2 attached to the sapphire substrate, while the other having WS_2 attached to the sapphire substrate. **Figure 4.3.1** shows the optical images of both the samples we fabricated.

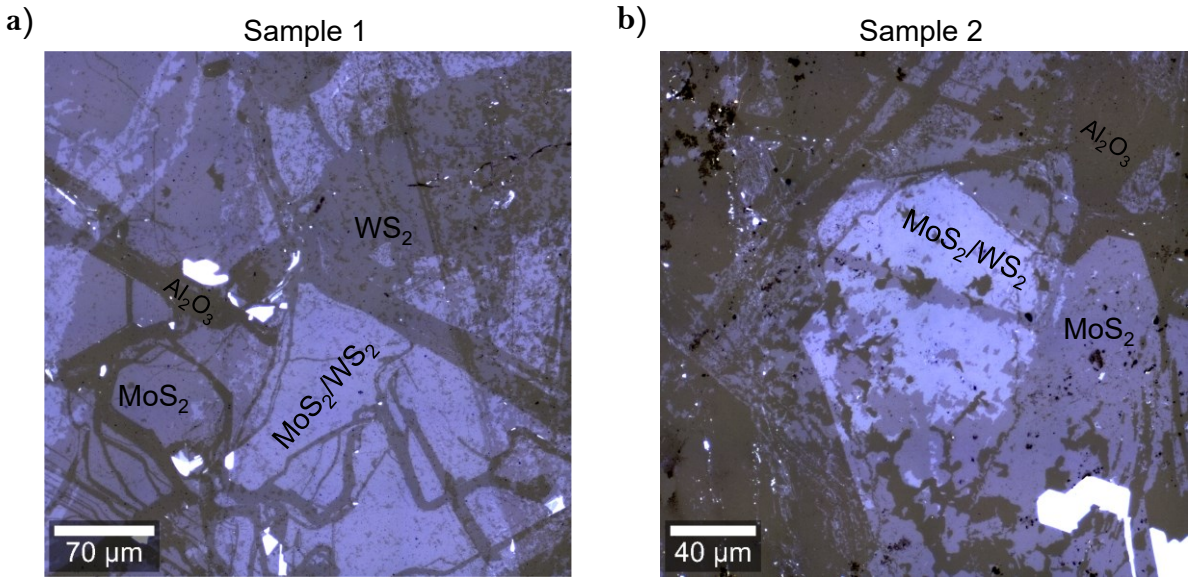

Figure 4.10 a), b): MoS_2/WS_2 heterostructure samples fabricated using the GAE method.

Although it is not clearly evident from these images as to which parts are individual monolayers and heterostructures, we perform Raman characterization to identify these regions, as discussed in the next section.

4.3.2 Characterization of the Heterostructure using Raman Spectroscopy

Using Raman spectroscopy, we were able to characterize our heterostructures by comparing with data from the literature [84]. We mainly observed the frequencies or the wavenumbers for the in-plane (E^1_{2g}) and out-of-plane (A_{1g}) vibrations of both monolayers, which were observable in the same Raman spectra at their specific positions. For both samples, the results were similar, and hence we only show the results for one of them, name Sample 1. **Figure 4.11** shows the Raman spectra at the positions of the two monolayer MoS_2 and WS_2, and also at the position of the MoS_2/WS_2 heterostructure.

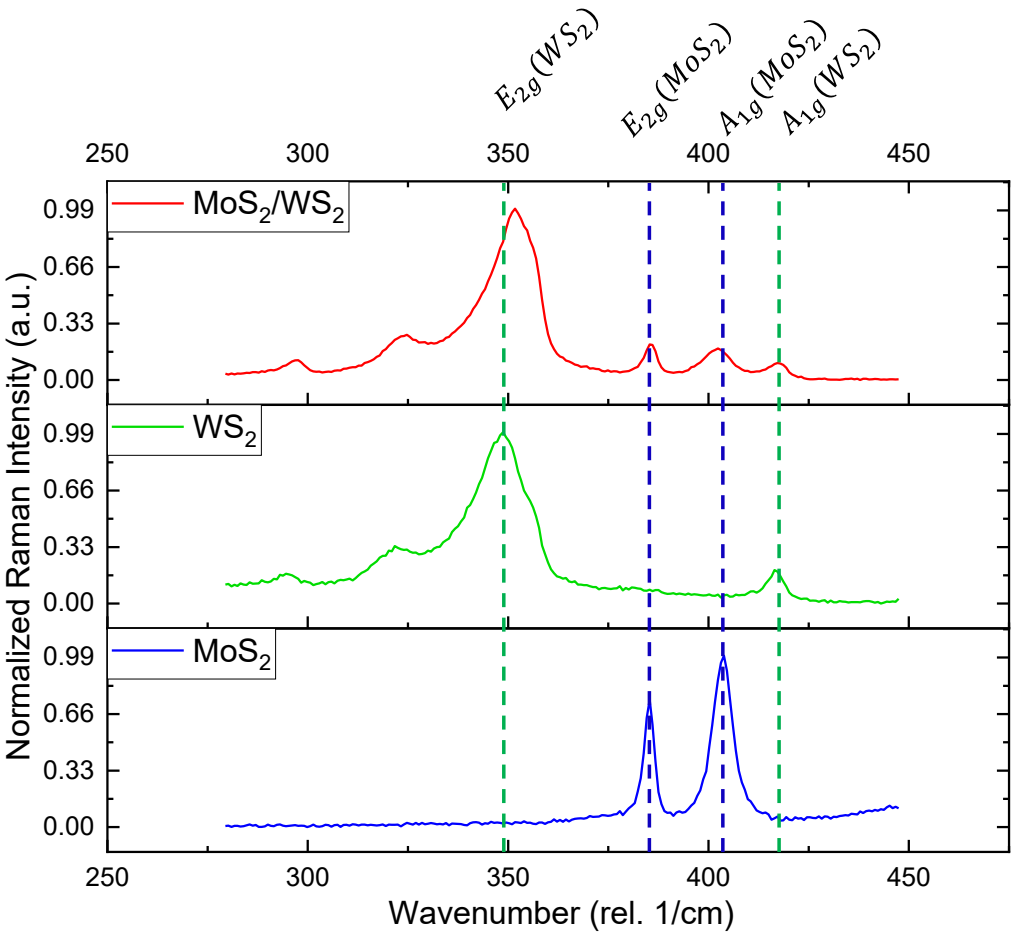

Figure 4.11: Raman spectra at three different positions in the sample corresponding the MoS_2/WS_2 heterostructure (*red*), WS_2 monolayer (*green*) and MoS_2 monolayer (*blue*).

As can be seen, the figure above suggests that at the position of the MoS_2/WS_2 heterostructure, the in-plane and out-of-plane Raman modes for both materials are present. This is consistent with previous literature [85,86]. However, it is important to mention that this Raman data does not provide much information on the level of coupling between the two monolayers. Hence, we used PL spectroscopy to qualitatively evaluate the interaction and the level of coupling in these MoS_2/WS_2 heterostructures.

4.3.3 PL Spectroscopy for Heterostructure Samples

As discussed in section **2.5**, due to the formation of interlayer excitons in MoS_2/WS_2 heterostructures, the probability of radiative recombination of these excitons significantly decreases. This is because the electron and the hole reside in different monolayers and also have different momenta. Hence, a significant quenching of the PL spectra is an indicator of optimal coupling and efficient charge transfer mechanism between the two individual monolayers. **Figure 4.12** presents

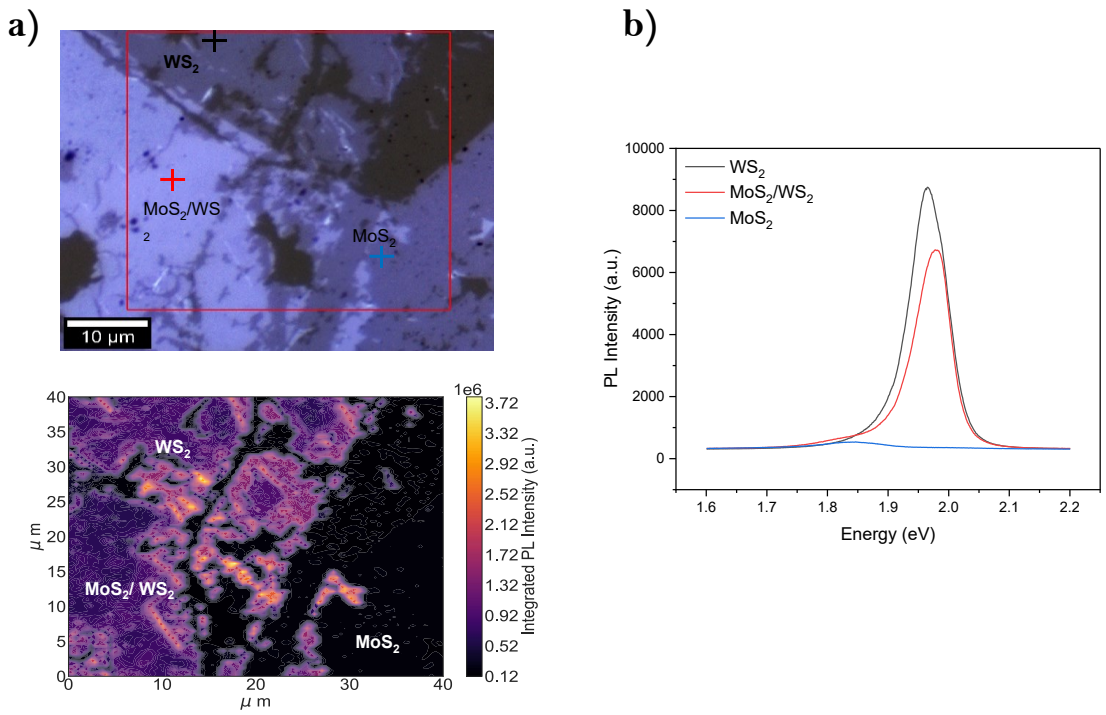

Figure 4.12: **a)** Area on the sample containing the monolayers of MoS_2 and WS_2 and also the MoS_2/WS_2 heterostructure; **b)** Single spectrum taken at specific spots in the sample corresponding to the two monolayers and the heterostructure

the PL data obtained from a sample containing MoS_2/WS_2 heterostructures, MoS_2 monolayer, and WS_2 monolayer. By analyzing single spectra from specific positions corresponding to the individual layers and the heterostructure, we do observe quenching of the PL in the heterostructure compared to the WS_2 monolayer, but a slight enhancement in the MoS_2 monolayer. However, contrary to previous literature reports, the quenching of the PL, corresponding to the A-exciton energy of the WS_2 monolayer, is not significant. To gain a broader perspective, we conducted PL mapping over an area of 1600 μm^2, covering all three materials (**Figure 4.12 a)**). Interestingly, we found that the PL quenching across the entire heterostructure area was not considerably high. We speculate that this observation could be attributed to lower coupling between the MoS_2 and WS_2 monolayers, resulting in minimal charge transfer.

Our speculation is based on the potential presence of contaminants accumulated on the surface of the first monolayer (WS_2) during the heterostructure fabrication process. This non-uniform contact between the two monolayers may have hindered efficient charge transfer between them, thereby explaining the absence of uniform and pronounced PL quenching in the fabricated heterostructures. However, we believe further optimization techniques will allow to enhance the quality of contact between the two layers, thereby promoting efficient charge transfer between them.

4.4 Exfoliation of ReS_2 and $ReSe_2$

We also applied the GAE method for exfoliating two other materials: **i)** ReS_2; and **ii)** $ReSe_2$. In **Figure 4.13**, the optical images are shown on the left where the crosses refer to positions where the Raman spectra of different layer numbers of both ReS_2 and $ReSe_2$ are taken and shown on extreme right. In the center, we show the images with a blue filter and increased contrast to identify the

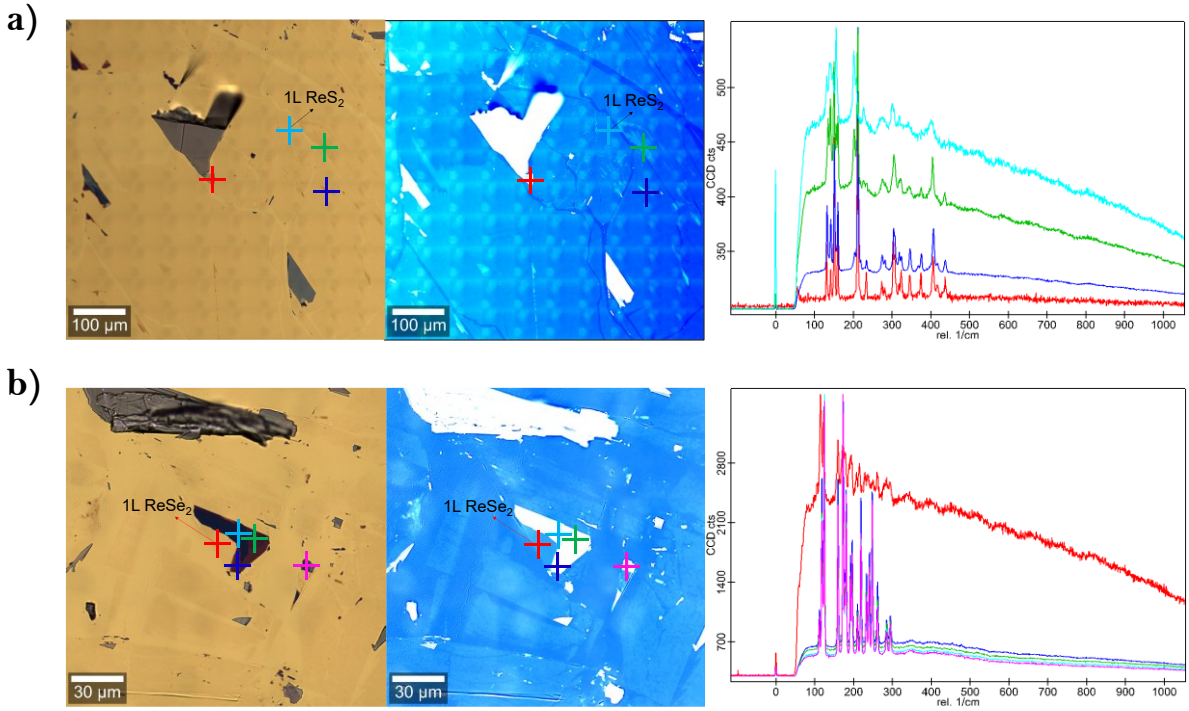

Figure 4.13: **a)** ReS_2 on gold. Colored crosses are the optical image correspond to the single-spectrums shown on the right. The Raman spectrum for monolayer is given in light blue; **b)** $ReSe_2$ on gold. Raman spectrum for monolayer is given in red.

regions where the materials are present. The faded white positions in the contrasted images are essentially where the monolayers are present. Higher contrast refer to more layer numbers of both these material, with the fully white positions referring to bulk and multilayer ReS_2.

This essentially shows that our method can be effectively extended to other layered materials as well. We also briefly analyzed the Raman and PL spectra for ReS_2 on and off gold, the results of which are displayed in **Appendix A7**. However, an in-depth analysis of both ReS_2 and $ReSe_2$ was not performed in this project due to time-constraints. Also, their anisotropic and highly sensitive optoelectronic behavior require more systematic and sophisticated measurements which was beyond the scope of this project.

Chapter 5

Conclusion and Future Outlook

Our study focused on the fabrication and characterization of large-area and high-quality monolayers of 2D TMDCs such as MoS_2 and WS_2, using the gold-assisted exfoliation method. We have successfully obtained monolayers of MoS_2 and WS_2 and have verified them using optical microscopy and Raman spectroscopy. We also assessed their quality through PL spectroscopy and compared it with commercially available CVD samples and mechanically exfoliated samples. This comparison demonstrated that our fabricated monolayers are of superior quality as compared to CVD samples and are of much larger area as compared to mechanically exfoliated ones. Notably, the quality of our WS_2 monolayers was extremely close to that of mechanically exfoliated samples.

We extended the gold-assisted exfoliation method to fabricate MoS_2/WS_2 heterostructures. Raman analysis confirmed the formation of heterostructures; however, we observed limited quenching of the PL spectra. This suggests a suboptimal contact between the two monolayers, leading to insufficient charge transfer. We anticipate that further optimization of the heterostructure fabrication process will enhance charge transfer efficiency and result in significant PL quenching.

Our results highlight the effectiveness of the gold-assisted exfoliation method for producing high-quality monolayers of 2D TMDCs, as well as their heterostructures. Additionally, we explored the exfoliation of two other materials, ReS_2 and $ReSe_2$, with preliminary results briefly presented in **Appendix A7**. These findings provide valuable insights and lay the groundwork for future research endeavors aimed at optimizing the fabrication process.

Moving forward, several avenues can be explored with these materials. Firstly, optimizing the heterostructure fabrication process is essential to improve the contact quality and enable efficient charge transfer. Secondly, the study of single-quantum emitters in these materials holds great promise for applications in quantum information processing and sensing. Understanding and manipulating the properties of defects and imperfections within the monolayers and heterostructures can enable the realization of robust and controllable quantum emitters.

Moreover, the gold-assisted exfoliation method can be extended to exfoliate other 2D materials beyond MoS_2 and WS_2. Exploring the compatibility of this method with a wide range of 2D materials will expand the toolkit for synthesizing diverse materials and heterostructures, unlocking new opportunities for fundamental research and technological applications.

References

(1) *IEA (2022), Solar PV, IEA, Paris*. IEA.

(2) Ballif, C.; Haug, F. J.; Boccard, M.; Verlinden, P. J.; Hahn, G. Status and Perspectives of Crystalline Silicon Photovoltaics in Research and Industry. *Nature Reviews Materials 2022 7:8* **2022**, *7* (8), 597–616.

(3) Andreani, L. C.; Bozzola, A.; Kowalczewski, P.; Liscidini, M.; Redorici, L. Silicon Solar Cells: Toward the Efficiency Limits. **2018**, *4* (1), 1548305.

(4) Zhao, Y.; Ouyang, G. Thickness-Dependent Photoelectric Properties of MoS2/Si Heterostructure Solar Cells. *Scientific Reports 2019 9:1* **2019**, *9* (1), 1–11.

(5) Okada, M.; Okada, N.; Chang, W. H.; Endo, T.; Ando, A.; Shimizu, T.; Kubo, T.; Miyata, Y.; Irisawa, T. Gas-Source CVD Growth of Atomic Layered WS2 from WF6 and H2S Precursors with High Grain Size Uniformity. *Scientific Reports 2019 9:1* **2019**, *9* (1), 1–10.

(6) Jariwala, D.; Sangwan, V. K.; Lauhon, L. J.; Marks, T. J.; Hersam, M. C. Emerging Device Applications for Semiconducting Two-Dimensional Transition Metal Dichalcogenides. *ACS Nano* **2014**, *8* (2), 1102–1120.

(7) Butler, S. Z.; Hollen, S. M.; Cao, L.; Cui, Y.; Gupta, J. A.; Gutiérrez, H. R.; Heinz, T. F.; Hong, S. S.; Huang, J.; Ismach, A. F.; Johnston-Halperin, E.; Kuno, M.; Plashnitsa, V. V.; Robinson, R. D.; Ruoff, R. S.; Salahuddin, S.; Shan, J.; Shi, L.; Spencer, M. G.; Terrones, M.; Windl, W.; Goldberger, J. E. Progress, Challenges, and Opportunities in Two-Dimensional Materials beyond Graphene. *ACS Nano* **2013**, *7* (4), 2898–2926.

(8) Mamta; Singh, Y.; Maurya, K. K.; Singh, V. N. Transition Metal Dichalcogenide MXY (M = Mo, W; X, Y = S, Se) Monolayer: Structure, Fabrication, Properties, and Applications. *J Mater Res* **2022**, *37* (20), 3403–3417.

(9) Wurstbauer, U.; Miller, B.; Parzinger, E.; Holleitner, A. W. Light–Matter Interaction in Transition Metal Dichalcogenides and Their Heterostructures. *J Phys D Appl Phys* **2017**, *50* (17), 173001.

(10) Li, H.; Wu, J.; Yin, Z.; Zhang, H. Preparation and Applications of Mechanically Exfoliated Single-Layer and Multilayer MoS2 and WSe2 Nanosheets. *Acc Chem Res* **2014**, *47* (4), 1067–1075.

(11) Sun, J.; Li, X.; Guo, W.; Zhao, M.; Fan, X.; Dong, Y.; Xu, C.; Deng, J.; Fu, Y. Synthesis Methods of Two-Dimensional MoS2: A Brief Review. *Crystals*. MDPI AG July 1, 2017. https://doi.org/10.3390/cryst7070198.

(12) Heyl, M.; List-Kratochvil, E. J. W. Only Gold Can Pull This off: Mechanical Exfoliations of Transition Metal Dichalcogenides beyond Scotch Tape. *Appl Phys A Mater Sci Process* **2023**, *129* (1), 1–17.

(13) Velický, M.; Donnelly, G. E.; Hendren, W. R.; McFarland, S.; Scullion, D.; DeBenedetti, W. J. I.; Correa, G. C.; Han, Y.; Wain, A. J.; Hines, M. A.; Muller, D. A.; Novoselov, K. S.; Abruña, H. D.; Bowman, R. M.; Santos, E. J. G.; Huang, F. Mechanism of Gold-Assisted Exfoliation of Centimeter-Sized Transition-Metal Dichalcogenide Monolayers. *ACS Nano* **2018**, *12* (10), 10463–10472.

(14) Huang, Y.; Pan, Y. H.; Yang, R.; Bao, L. H.; Meng, L.; Luo, H. L.; Cai, Y. Q.; Liu, G. D.; Zhao, W. J.; Zhou, Z.; Wu, L. M.; Zhu, Z. L.; Huang, M.; Liu, L. W.; Liu, L.; Cheng, P.; Wu, K. H.; Tian, S. B.; Gu, C. Z.; Shi, Y. G.; Guo, Y. F.; Cheng, Z. G.; Hu, J. P.; Zhao, L.; Yang, G. H.; Sutter, E.; Sutter, P.; Wang, Y. L.; Ji, W.; Zhou, X. J.; Gao, H. J. Universal Mechanical Exfoliation of Large-Area 2D Crystals. *Nature Communications 2020 11:1* **2020**, *11* (1), 1–9.

(15) Chhowalla, M.; Shin, H. S.; Eda, G.; Li, L. J.; Loh, K. P.; Zhang, H. The Chemistry of Two-Dimensional Layered Transition Metal Dichalcogenide Nanosheets. *Nature Chemistry 2013 5:4* **2013**, *5* (4), 263–275.

(16) Wang, Q. H.; Kalantar-Zadeh, K.; Kis, A.; Coleman, J. N.; Strano, M. S. Electronics and Optoelectronics of Two-Dimensional Transition Metal Dichalcogenides. *Nature Nanotechnology 2012 7:11* **2012**, *7* (11), 699–712.

(17) Manzeli, S.; Ovchinnikov, D.; Pasquier, D.; Yazyev, O. V.; Kis, A. 2D Transition Metal Dichalcogenides. *Nature Reviews Materials 2017 2:8* **2017**, *2* (8), 1–15.

(18) Chhowalla, M.; Shin, H. S.; Eda, G.; Li, L. J.; Loh, K. P.; Zhang, H. The Chemistry of Two-Dimensional Layered Transition Metal Dichalcogenide Nanosheets. *Nature Chemistry 2013 5:4* **2013**, *5* (4), 263–275.

(19) Tongay, S.; Sahin, H.; Ko, C.; Luce, A.; Fan, W.; Liu, K.; Zhou, J.; Huang, Y. S.; Ho, C. H.; Yan, J.; Ogletree, D. F.; Aloni, S.; Ji, J.; Li, S.; Li, J.; Peeters, F. M.; Wu, J. Monolayer Behaviour in Bulk ReS2 Due to Electronic and Vibrational Decoupling. *Nature Communications 2014 5:1* **2014**, *5* (1), 1–6.

(20) Liu, G. Bin; Xiao, D.; Yao, Y.; Xu, X.; Yao, W. Electronic Structures and Theoretical Modelling of Two-Dimensional Group-VIB Transition Metal Dichalcogenides. *Chem Soc Rev* **2015**, *44* (9), 2643–2663.

(21) Zhao, W.; Ribeiro, R. M.; Toh, M.; Carvalho, A.; Kloc, C.; Castro Neto, A. H.; Eda, G. Origin of Indirect Optical Transitions in Few-Layer MoS2, WS2, and WSe2. *Nano Lett* **2013**, *13* (11), 5627–5634.

(22) Wang, Q. H.; Kalantar-Zadeh, K.; Kis, A.; Coleman, J. N.; Strano, M. S. Electronics and Optoelectronics of Two-Dimensional Transition Metal Dichalcogenides. *Nature Nanotechnology 2012 7:11* **2012**, *7* (11), 699–712.

(23) Liu, G. Bin; Xiao, D.; Yao, Y.; Xu, X.; Yao, W. Electronic Structures and Theoretical Modelling of Two-Dimensional Group-VIB Transition Metal Dichalcogenides. *Chem Soc Rev* **2015**, *44* (9), 2643–2663.

(24) Liu, G. Bin; Shan, W. Y.; Yao, Y.; Yao, W.; Xiao, D. Three-Band Tight-Binding Model for Monolayers of Group-VIB Transition Metal Dichalcogenides. *Phys Rev B Condens Matter Mater Phys* **2013**, *88* (8), 085433.

(25) Kuc, A.; Zibouche, N.; Heine, T. Influence of Quantum Confinement on the Electronic Structure of the Transition Metal Sulfide TS2. *Phys Rev B Condens Matter Mater Phys* **2011**, *83* (24), 245213.

(26) Li, T.; Galli, G. Electronic Properties of MoS 2 Nanoparticles. *Journal of Physical Chemistry C* **2007**, *111* (44), 16192–16196.

(27) Cheiwchanchamnangij, T.; Lambrecht, W. R. L. Quasiparticle Band Structure Calculation of Monolayer, Bilayer, and Bulk MoS 2. *Phys Rev B Condens Matter Mater Phys* **2012**, *85* (20).

(28) Zeng, H.; Liu, G. Bin; Dai, J.; Yan, Y.; Zhu, B.; He, R.; Xie, L.; Xu, S.; Chen, X.; Yao, W.; Cui, X. Optical Signature of Symmetry Variations and Spin-Valley Coupling in Atomically Thin Tungsten Dichalcogenides. *Sci Rep* **2013**, *3*.

(29) Wang, G.; Chernikov, A.; Glazov, M. M.; Heinz, T. F.; Marie, X.; Amand, T.; Urbaszek, B. Colloquium: Excitons in Atomically Thin Transition Metal Dichalcogenides. *Rev Mod Phys* **2018**, *90* (2).

(30) Huang, Y.; Pan, Y. H.; Yang, R.; Bao, L. H.; Meng, L.; Luo, H. L.; Cai, Y. Q.; Liu, G. D.; Zhao, W. J.; Zhou, Z.; Wu, L. M.; Zhu, Z. L.; Huang, M.; Liu, L. W.; Liu, L.; Cheng, P.; Wu, K. H.; Tian, S. B.; Gu, C. Z.; Shi, Y. G.; Guo, Y. F.; Cheng, Z. G.; Hu, J. P.; Zhao, L.; Yang, G. H.; Sutter, E.; Sutter, P.; Wang, Y. L.; Ji, W.; Zhou, X. J.; Gao, H. J. Universal Mechanical Exfoliation of Large-Area 2D Crystals. *Nature Communications 2020 11:1* **2020**, *11* (1), 1–9.

(31) Huang, X.; Zhang, L.; Liu, L.; Qin, Y.; Fu, Q.; Wu, Q.; Yang, R.; Lv, J. P.; Ni, Z.; Liu, L.; Ji, W.; Wang, Y.; Zhou, X.; Huang, Y. Raman Spectra Evidence for the Covalent-like Quasi-Bonding between Exfoliated MoS2 and Au Films. *Science China Information Sciences* **2021**, *64* (4), 1–9.

(32) Heyl, M.; Burmeister, D.; Schultz, T.; Pallasch, S.; Ligorio, G.; Koch, N.; List-Kratochvil, E. J. W. Thermally Activated Gold-Mediated Transition Metal Dichalcogenide Exfoliation and a Unique Gold-Mediated Transfer. *Physica Status Solidi - Rapid Research Letters* **2020**, *14* (11).

(33) *Semiconductor Optics, Claus F. Klingshirn*

(34) *Introduction to Solid State Physics Charles Kittel*; 2005.

(35) Zheng, X.; Zhang, X.; Zheng, X.; Zhang, X. Excitons in Two-Dimensional Materials. *Advances in Condensed-Matter and Materials Physics - Rudimentary Research to Topical Technology* **2019**.

(36) Chernikov, A.; Berkelbach, T. C.; Hill, H. M.; Rigosi, A.; Li, Y.; Aslan, O. B.; Reichman, D. R.; Hybertsen, M. S.; Heinz, T. F. Exciton Binding Energy and Nonhydrogenic Rydberg Series in Monolayer WS2. *Phys Rev Lett* **2014**, *113* (7), 076802.

(37) Lynch, J.; Guarneri, L.; Jariwala, D.; Van De Groep, J. Exciton Resonances for Atomically-Thin Optics. *J Appl Phys* **2022**, *132* (9).

(38) Xiao, J.; Zhao, M.; Wang, Y.; Zhang, X. Excitons in Atomically Thin 2D Semiconductors and Their Applications. *Nanophotonics*. Walter de Gruyter GmbH 2017, pp 1309–1328.

(39) Kezerashvili, R. Y. Few-Body Systems in Condensed Matter Physics. *Few Body Syst* **2019**, *60* (3), 1–24.

(40) Mueller, T.; Malic, E. Exciton Physics and Device Application of Two-Dimensional Transition Metal Dichalcogenide Semiconductors. *npj 2D Materials and Applications 2018 2:1* **2018**, *2* (1), 1–12..

(41) Mak, K. F.; He, K.; Lee, C.; Lee, G. H.; Hone, J.; Heinz, T. F.; Shan, J. Tightly Bound Trions in Monolayer MoS2. *Nature Materials 2012 12:3* **2012**, *12* (3), 207–211.

(42) You, Y.; Zhang, X. X.; Berkelbach, T. C.; Hybertsen, M. S.; Reichman, D. R.; Heinz, T. F. Observation of Biexcitons in Monolayer WSe2. *Nature Physics 2014 11:6* **2015**, *11* (6), 477–481.

(43) Shang, J.; Shen, X.; Cong, C.; Peimyoo, N.; Cao, B.; Eginligil, M.; Yu, T. Observation of Excitonic Fine Structure in a 2D Transition-Metal Dichalcogenide Semiconductor. *ACS Nano* **2015**, *9* (1), 647–655.

(44) Fries, F.; Reineke, S. Statistical Treatment of Photoluminescence Quantum Yield Measurements. *Scientific Reports 2019 9:1* **2019**, *9* (1), 1–6.

(45) Liu, X. K.; Xu, W.; Bai, S.; Jin, Y.; Wang, J.; Friend, R. H.; Gao, F. Metal Halide Perovskites for Light-Emitting Diodes. *Nature Materials 2020 20:1* **2020**, *20* (1), 10–21.

(46) Greben, K.; Arora, S.; Harats, M. G.; Bolotin, K. I. Intrinsic and Extrinsic Defect-Related Excitons in TMDCs. *Nano Lett* **2020**, *20* (4), 2544–2550.

(47) Gong, X.; Voznyy, O.; Jain, A.; Liu, W.; Sabatini, R.; Piontkowski, Z.; Walters, G.; Bappi, G.; Nokhrin, S.; Bushuyev, O.; Yuan, M.; Comin, R.; McCamant, D.; Kelley, S. O.; Sargent, E. H. Electron–Phonon Interaction in Efficient Perovskite Blue Emitters. *Nature Materials 2018 17:6* **2018**, *17* (6), 550–556.

(48) Zhou, M.; Wang, W.; Lu, J.; Ni, Z. How Defects Influence the Photoluminescence of TMDCs. *Nano Res* **2021**, *14* (1), 29–39.

(49) Moody, G.; Schaibley, J.; Xu, X. Exciton Dynamics in Monolayer Transition Metal Dichalcogenides. *Journal of the Optical Society of America B* **2016**, *33* (7), C39.

(50) Yuan, L.; Wang, T.; Zhu, T.; Zhou, M.; Huang, L. Exciton Dynamics, Transport, and Annihilation in Atomically Thin Two-Dimensional Semiconductors. *Journal of Physical Chemistry Letters*. American Chemical Society July 20, 2017, pp 3371–3379.

(51) Shi, H.; Yan, R.; Bertolazzi, S.; Brivio, J.; Gao, B.; Kis, A.; Jena, D.; Xing, H. G.; Huang, L. Exciton Dynamics in Suspended Monolayer and Few-Layer MoS2 2D Crystals. *ACS Nano* **2013**, *7* (2), 1072–1080.

(52) Thompson, T. *Fundamentals of Raman Spectroscopy*.

(53) Ferraro, J. R.; Nakamoto, K.; Brown, C. W. *Introductory Raman Spectroscopy*; Academic Press, 2003.

(54) Toporski, J.; Dieing, T.; Hollricher, O. *Confocal Raman Microscopy*; Vol. 66.

(55) Wieting, T. J.; Verble, J. L. Infrared and Raman Studies of Long-Wavelength Optical Phonons in Hexagonal MoS2. *Phys Rev B* **1971**, *3* (12), 4286–4292.

(56) Meaden, G. T.; Rao, K. V; Loo, H. Y.; Tee, K. T.; Legvold, S.; Rev, P.; Moore, J. P.; Williams, R. K.; McElroy, D. L.; Powell, R. W.; Ho, C. Y.; Liley, P. E.; Laubitz, M. J.; Flynn, D. R.; Peavy, B. A.; National Brueau, U. S.; Verble, J. L.; Wieting, T. J. *Lorenz-Number Peak at Tc of Dysprosium; Thermal-Conductivity Extrema at T, of Erbium). 6S. Arajs and G. R. Dunmyre*; 1969; Vol. 25.

(57) Lucovsky, G.; White, R. M.; Benda, J. A.; Revelli, J. F. *Infrared-Reflectance Spectra of Layered Group-IV and Group-VI Transition-Metal Dichalcogenides*; 1973; Vol. 7.

(58) Yin, P.; Lin, Q.; Duan, Y. Applications of Raman Spectroscopy in Two-Dimensional Materials. *Journal of Innovative Optical Health Sciences*. World Scientific September 1, 2020.

(59) Liang, F.; Xu, H.; Wu, X.; Wang, C.; Luo, C.; Zhang, J. Raman Spectroscopy Characterization of Two-Dimensional Materials. *Chinese Physics B*. Institute of Physics Publishing March 1, 2018.

(60) Geim, A. K.; Grigorieva, I. V. Van Der Waals Heterostructures. *Nature 2013 499:7459* **2013**, *499* (7459), 419–425.

(61) Kolobov, A. V; Tominaga, J. *Springer Series in Materials Science 239 Two-Dimensional Transition-Metal Dichalcogenides*. http://www.springer.com/series/856.

(62) Chen, Y.; Sun, M. Two-Dimensional WS2/MoS2heterostructures: Properties and Applications. *Nanoscale*. Royal Society of Chemistry March 21, 2021, pp 5594–5619.

(63) Komsa, H. P.; Krasheninnikov, A. V. Electronic Structures and Optical Properties of Realistic Transition Metal Dichalcogenide Heterostructures from First Principles. *Phys Rev B Condens Matter Mater Phys* **2013**, *88* (8), 085318.

(64) Li, W.; Wang, T.; Dai, X.; Wang, X.; Zhai, C.; Ma, Y.; Chang, S.; Tang, Y. Electric Field Modulation of the Band Structure in MoS2/WS2 van Der Waals Heterostructure. *Solid State Commun* **2017**, *250*, 9–13.

(65) Tongay, S.; Fan, W.; Kang, J.; Park, J.; Koldemir, U.; Suh, J.; Narang, D. S.; Liu, K.; Ji, J.; Li, J.; Sinclair, R.; Wu, J. Tuning Interlayer Coupling in Large-Area Heterostructures with CVD-Grown MoS2 and WS2 Monolayers. *Nano Lett* **2014**, *14* (6), 3185–3190.

(66) Jin, C.; Ma, E. Y.; Karni, O.; Regan, E. C.; Wang, F.; Heinz, T. F. Ultrafast Dynamics in van Der Waals Heterostructures. *Nature Nanotechnology 2018 13:11* **2018**, *13* (11), 994–1003.

(67) Hong, X.; Kim, J.; Shi, S. F.; Zhang, Y.; Jin, C.; Sun, Y.; Tongay, S.; Wu, J.; Zhang, Y.; Wang, F. Ultrafast Charge Transfer in Atomically Thin MoS2/WS2 Heterostructures. *Nature Nanotechnology 2014 9:9* **2014**, *9* (9), 682–686.

(68) Kozawa, D.; Carvalho, A.; Verzhbitskiy, I.; Giustiniano, F.; Miyauchi, Y.; Mouri, S.; Castro Neto, A. H.; Matsuda, K.; Eda, G. Evidence for Fast Interlayer Energy Transfer in MoSe2/WS2 Heterostructures. *Nano Lett* **2016**, *16* (7), 4087–4093.

(69) Xu, W.; Kozawa, D.; Liu, Y.; Sheng, Y.; Wei, K.; Koman, V. B.; Wang, S.; Wang, X.; Jiang, T.; Strano, M. S.; Warner, J. H.; Xu, W.; Sheng, Y.; Wang, S.; Wang, X.; Warner, J. H.; Kozawa, D.; Koman, V. B.; Strano, M. S.; Liu, Y.; Wei, K.; Jiang, T. Determining the Optimized Interlayer Separation Distance in Vertical Stacked 2D WS2:HBN:MoS2 Heterostructures for Exciton Energy Transfer. *Small* **2018**, *14* (13), 1703727.

(70) Liu, F.; Wu, W.; Bai, Y.; Chae, S. H.; Li, Q.; Wang, J.; Hone, J.; Zhu, X.-Y. *Disassembling 2D van Der Waals Crystals into Macroscopic Monolayers and Reassembling into Artificial Lattices*.

(71) Kennes, D. M.; Claassen, M.; Xian, L.; Georges, A.; Millis, A. J.; Hone, J.; Dean, C. R.; Basov, D. N.; Pasupathy, A. N.; Rubio, A. Moiré Heterostructures as a Condensed-Matter Quantum Simulator. *Nature Physics*. Nature Research February 1, 2021, pp 155–163.

(72) Guan, L.; Xing, B.; Niu, X.; Wang, D.; Yu, Y.; Zhang, S.; Yan, X.; Wang, Y.; Sha, J. Metal-Assisted Exfoliation of Few-Layer Black Phosphorus with High Yield. *Chemical Communications* **2018**, *54* (6), 595–598.

(73) Li, S.; Pam, M. E.; Li, Y.; Chen, L.; Chien, Y. C.; Fong, X.; Chi, D.; Ang, K. W. Wafer-Scale 2D Hafnium Diselenide Based Memristor Crossbar Array for Energy-Efficient Neural Network Hardware. *Advanced Materials* **2022**, *34* (25).

(74) Magda, G. Z.; Petõ, J.; Dobrik, G.; Hwang, C.; Biró, L. P.; Tapasztó, L. Exfoliation of Large-Area Transition Metal Chalcogenide Single Layers. *Sci Rep* **2015**, *5*.

(75) Johnson, N. Lloyd.; Kotz, Samuel.; Balakrishnan, N. *Continuous Univariate Distributions*; Wiley, 1994.

(76) Li, H.; Zhang, Q.; Yap, C. C. R.; Tay, B. K.; Edwin, T. H. T.; Olivier, A.; Baillargeat, D. From Bulk to Monolayer MoS2: Evolution of Raman Scattering. *Adv Funct Mater* **2012**, *22* (7), 1385–1390.

(77) Velický, M.; Rodriguez, A.; Bouša, M.; Krayev, A. V.; Vondráček, M.; Honolka, J.; Ahmadi, M.; Donnelly, G. E.; Huang, F.; Abrunã, H. D.; Novoselov, K. S.; Frank, O. Strain and Charge Doping Fingerprints of the Strong Interaction between Monolayer MoS2and Gold. *Journal of Physical Chemistry Letters* **2020**, *11* (15), 6112–6118.

(78) Qiao, S.; Yang, H.; Bai, Z.; Peng, G.; Zhang, X. *Identifying the Number of WS 2 Layers via Raman and Photoluminescence Spectrum*; 2017.

(79) Bhanu, U.; Islam, M. R.; Tetard, L.; Khondaker, S. I. Photoluminescence Quenching in Gold - MoS2 Hybrid Nanoflakes. *Scientific Reports 2014 4:1* **2014**, *4* (1), 1–5.

(80) Selig, M.; Berghäuser, G.; Raja, A.; Nagler, P.; Schüller, C.; Heinz, T. F.; Korn, T.; Chernikov, A.; Malic, E.; Knorr, A. Excitonic Linewidth and Coherence Lifetime in Monolayer Transition Metal Dichalcogenides. *Nat Commun* **2016**, *7*.

(81) Ayari, S.; Jaziri, S. Dynamics of Free and Localized Excitons in Two-Dimensional Transition Metal Dichalcogenides. *Phys Status Solidi B Basic Res* **2019**, *256* (6).

(82) Yang, L.; Cui, X.; Zhang, J.; Wang, K.; Shen, M.; Zeng, S.; Dayeh, S. A.; Feng, L.; Xiang, B. Lattice Strain Effects on the Optical Properties of MoS2 Nanosheets. *Scientific Reports 2014 4:1* **2014**, *4* (1), 1–7.

(83) McCreary, K. M.; Hanbicki, A. T.; Sivaram, S. V.; Jonker, B. T. A- and B-Exciton Photoluminescence Intensity Ratio as a Measure of Sample Quality for Transition Metal Dichalcogenide Monolayers. *APL Mater* **2018**, *6* (11), 111106.

(84) Lin, X.; Wang, F.; Shen, J.; Di, X.; Di, H.; Yan, M.; Zhang, K. Synthesis of Mos2/Ws2Vertical Heterostructure and Its Photoelectric Properties. In *China Semiconductor Technology International Conference 2020, CSTIC 2020*; Institute of Electrical and Electronics Engineers Inc., 2020.

(85) Liang, L.; Meunier, V. First-Principles Raman Spectra of MoS2, WS2 and Their Heterostructures. *Nanoscale* **2014**, *6* (10), 5394–5401.

(86) Shin, K. H.; Seo, M. K.; Pak, S.; Jang, A. R.; Sohn, J. I. Observation of Strong Interlayer Couplings in WS2/MoS2 Heterostructures via Low-Frequency Raman Spectroscopy. *Nanomaterials* **2022**, *12* (9).

(87) Liu, E.; Fu, Y.; Wang, Y.; Feng, Y.; Liu, H.; Wan, X.; Zhou, W.; Wang, B.; Shao, L.; Ho, C. H.; Huang, Y. S.; Cao, Z.; Wang, L.; Li, A.; Zeng, J.; Song, F.; Wang, X.; Shi, Y.; Yuan, H.; Hwang, H. Y.; Cui, Y.; Miao, F.; Xing, D. Integrated Digital Inverters Based on Two-Dimensional Anisotropic ReS2 Field-Effect Transistors. *Nature Communications 2015 6:1* **2015**, *6* (1), 1–7.

(88) Wolverson, D.; Crampin, S.; Kazemi, A. S.; Ilie, A.; Bending, S. J. Raman Spectra of Monolayer, Few-Layer, and Bulk ReSe2: An Anisotropic Layered Semiconductor. *ACS Nano* **2014**, *8* (11), 11154–11164.

(89) Zhong, H. X.; Gao, S.; Shi, J. J.; Yang, L. Quasiparticle Band Gaps, Excitonic Effects, and Anisotropic Optical Properties of the Monolayer Distorted 1T Diamond-Chain Structures ReS2 and ReSe2. *Phys Rev B Condens Matter Mater Phys* **2015**, *92* (11), 115438.

(90) Yu, Z. G.; Cai, Y.; Zhang, Y. W. Robust Direct Bandgap Characteristics of One- and Two-Dimensional ReS2. *Scientific Reports 2015 5:1* **2015**, *5* (1), 1–9.

(91) Tongay, S.; Sahin, H.; Ko, C.; Luce, A.; Fan, W.; Liu, K.; Zhou, J.; Huang, Y. S.; Ho, C. H.; Yan, J.; Ogletree, D. F.; Aloni, S.; Ji, J.; Li, S.; Li, J.; Peeters, F. M.; Wu, J. Monolayer Behaviour in Bulk ReS2 Due to Electronic and Vibrational Decoupling. *Nature Communications 2014 5:1* **2014**, *5* (1), 1–6.

(92) Shubnic, A. A.; Polozkov, R. G.; Shelykh, I. A.; Iorsh, I. V. High Refractive Index and Extreme Biaxial Optical Anisotropy of Rhenium Diselenide for Applications in All-Dielectric Nanophotonics. *Nanophotonics* **2020**, *9* (16), 4737–4742.

(93) Hart, L. S.; Webb, J. L.; Dale, S.; Bending, S. J.; Mucha-Kruczynski, M.; Wolverson, D.; Chen, C.; Avila, J.; Asensio, M. C. Electronic Bandstructure and van Der Waals Coupling of ReSe2 Revealed by High-Resolution Angle-Resolved Photoemission Spectroscopy. *Scientific Reports 2017 7:1* **2017**, *7* (1), 1–9.

(94) Radisavljevic, B.; Radenovic, A.; Brivio, J.; Giacometti, V.; Kis, A. Single-Layer MoS2 Transistors. *Nature Nanotechnology 2011 6:3* **2011**, *6* (3), 147–150.

(95) Herman, A. P.; Zelewski, S. J.; Misztal, K.; Kudrawiec, R. Probing the Long-Lived Photo-Generated Charge Carriers in Transition Metal Dichalcogenides by Time-Resolved Microwave Photoconductivity. *Nanophotonics* **2022**, *11* (7), 1335–1344.

Appendix

A1. Band Structures of Group VII TMDCs (ReS_2 and $ReSe_2$)

Group VII TMDCs exhibit a distorted 1T-phase (or 1T'-phase) and their band structures for monolayer and bulk forms have been studied using first principle DFT calculations [87–91]. Although limited work has been done in calculating the band structures of these materials, DFT calculations have provided an approximate understanding of their band structures. ReS_2 is a direct bandgap material in both the bulk and monolayer form, and the bandgap increases from 1.35 eV in the bulk to 1.43 eV in the monolayer [91]. This is attributed to the electronically and vibrationally decoupled nature of the individual monolayers in the out-of-plane direction, which prevents band renormalization as the material is thinned down. These electronic transitions are Γ-Γ transitions in the k-space.

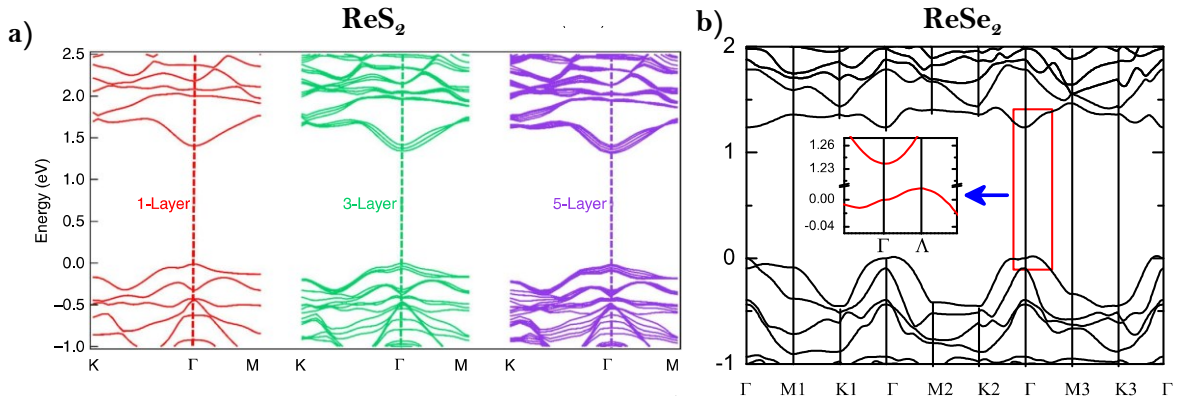

Figure A1: a) DFT calculated band structures of ReS_2 for different layer numbers [19]; **b)** DFT calculated band structures for $ReSe_2$ [89]

On the other hand, studies on $ReSe_2$ have suggested that the material has an indirect bandgap [88,89,92]. For $ReSe_2$ monolayers, CBM is located at the Γ-point while the VBM is slightly away from it. Nano-ARPES measurements have also indicated that there is an out-of-phase dispersion in $ReSe_2$, which implies appreciable van der Waals coupling among the individual layers in bulk $ReSe_2$, unlike in ReS_2 [93]. Consequently, the band structures of bulk and monolayer $ReSe_2$ are expected to be significantly different. Thus, there could be appreciable bandgap renormalization as the material is thinned down. Experimental studies have suggested that the indirect bandgap value of bulk $ReSe_2$ is in the range of 0.98 – 1.06 eV [88]. DFT calculations indicate that for $ReSe_2$ monolayers, the indirect bandgap value is around 1.22 eV and the direct bandgap at the Γ-point is around 1.25 eV [89].

A2. Charge Transfer from Monolayer to Gold

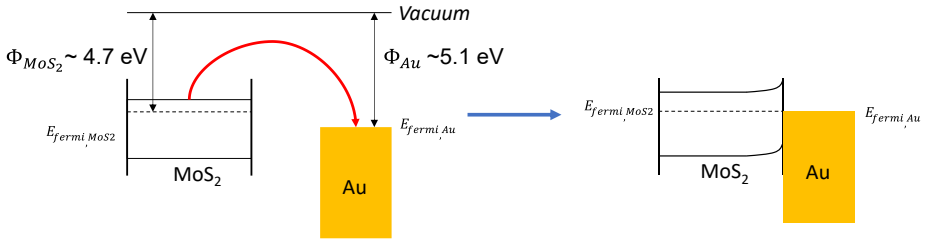

Figure A2: Charge transfer at metal-semiconductor junction in MoS_2/Au heterostructure. Schematic inspired from [79].

A3. Monolayer Behavior under Different Excitation Regimes

Our observations reveal that as the excitation laser power increases, the presence of trions in the monolayer samples of WS_2 and MoS_2 becomes increasingly apparent. This phenomenon can be attributed to the generation of free charges at higher laser powers, leading to Coulombic interactions with the A-excitons in the material and subsequently reducing their population. For a comprehensive representation, **Figure A1** display the normalized spectra of the MoS_2 and WS_2 monolayers as the laser power progressively increases. Hence, a notable increase is observed in the photoluminescence (PL) spectra emitted from the trions compared to the A-excitons under high laser powers. However, in the case of MoS_2, the PL from both A- and B- excitons seems to red-shift with increasing laser power under the curve-fitting procedure. The spikes in MoS_2 monolayer refer to background PL signals from the Al_2O_3 substrate.

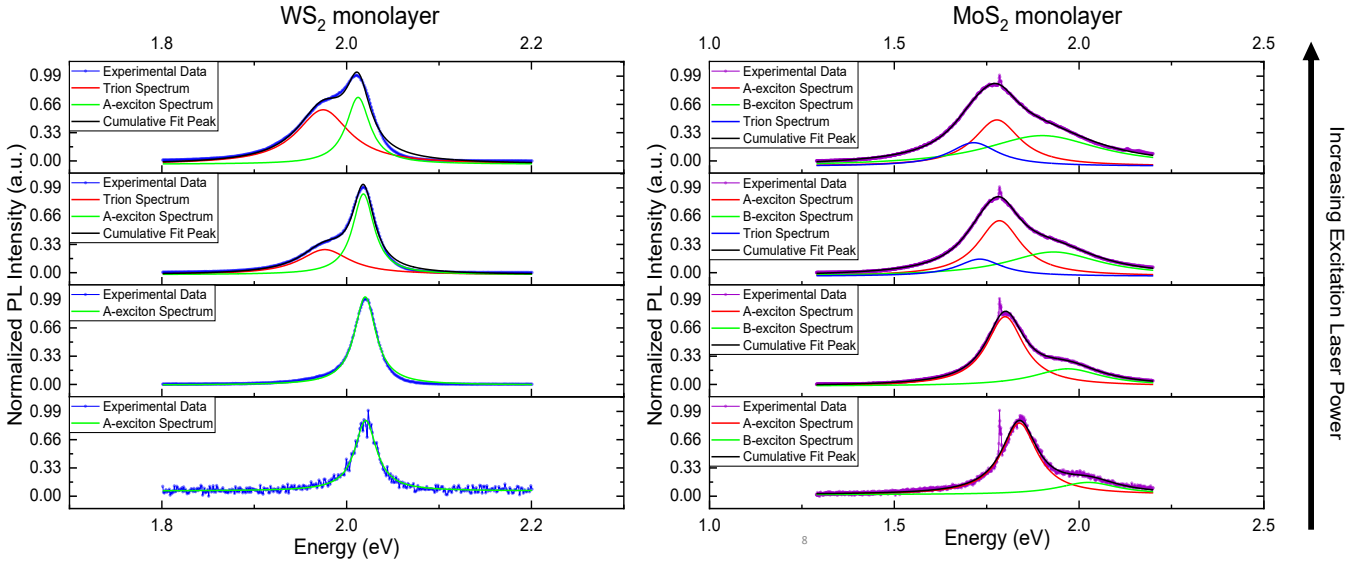

Figure A3: Normalized plots showing the trion formation at high excitation regimes.

A4. Analysis of PL spectra for WS_2

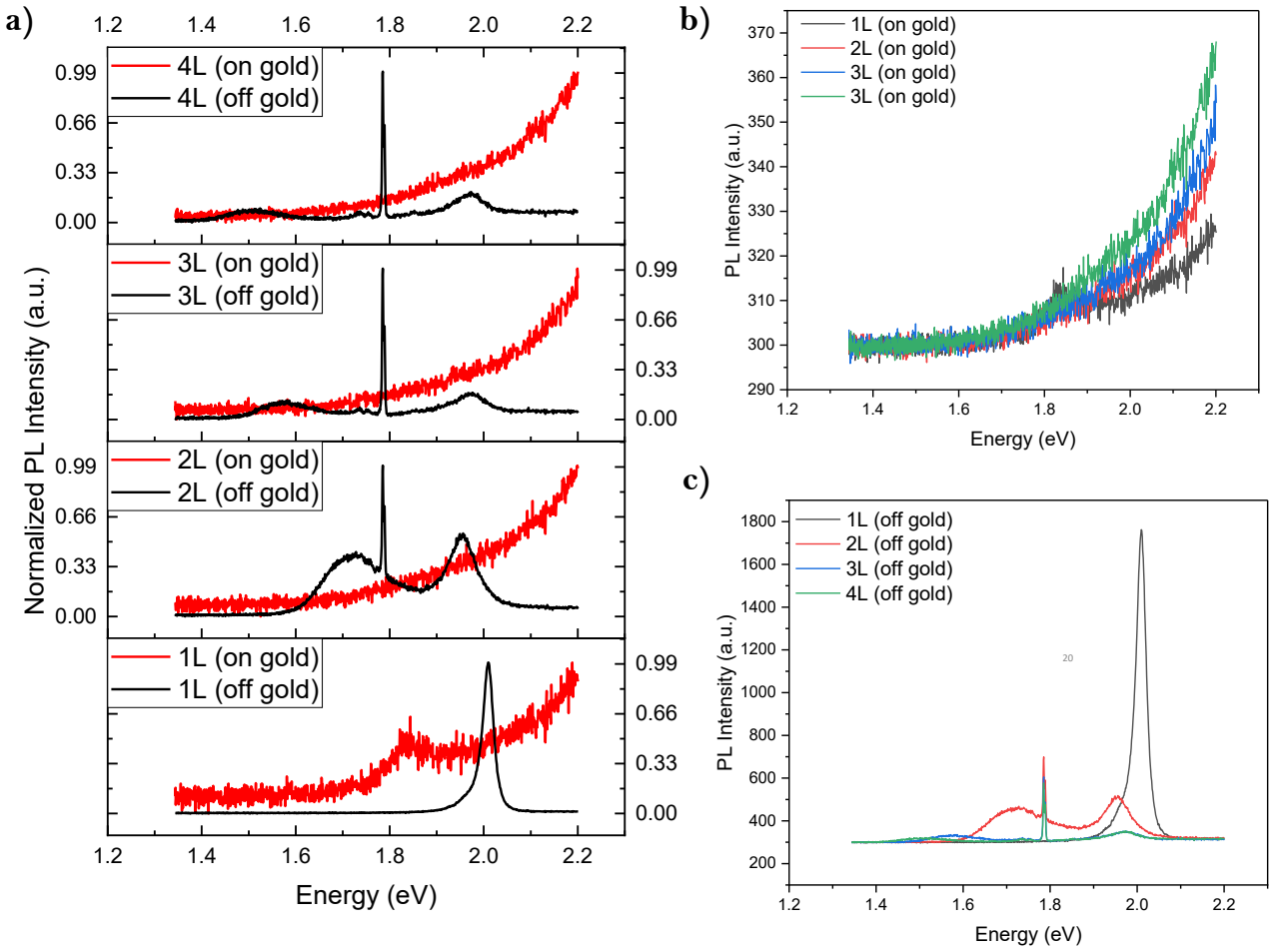

Figure A4.: **a)** Stacked plots for normalized PL spectra for WS_2 on and off gold; **b)** PL spectra for WS_2 on gold; **c)** PL spectra for WS_2 off gold. *Spikes in 2L, 3L and 4L WS_2 off gold, around 1.8 eV refer to background PL signal from sapphire substrate.*

A5. PL Spectra and Maps for CVD, GAE and PDMS samples for MoS_2

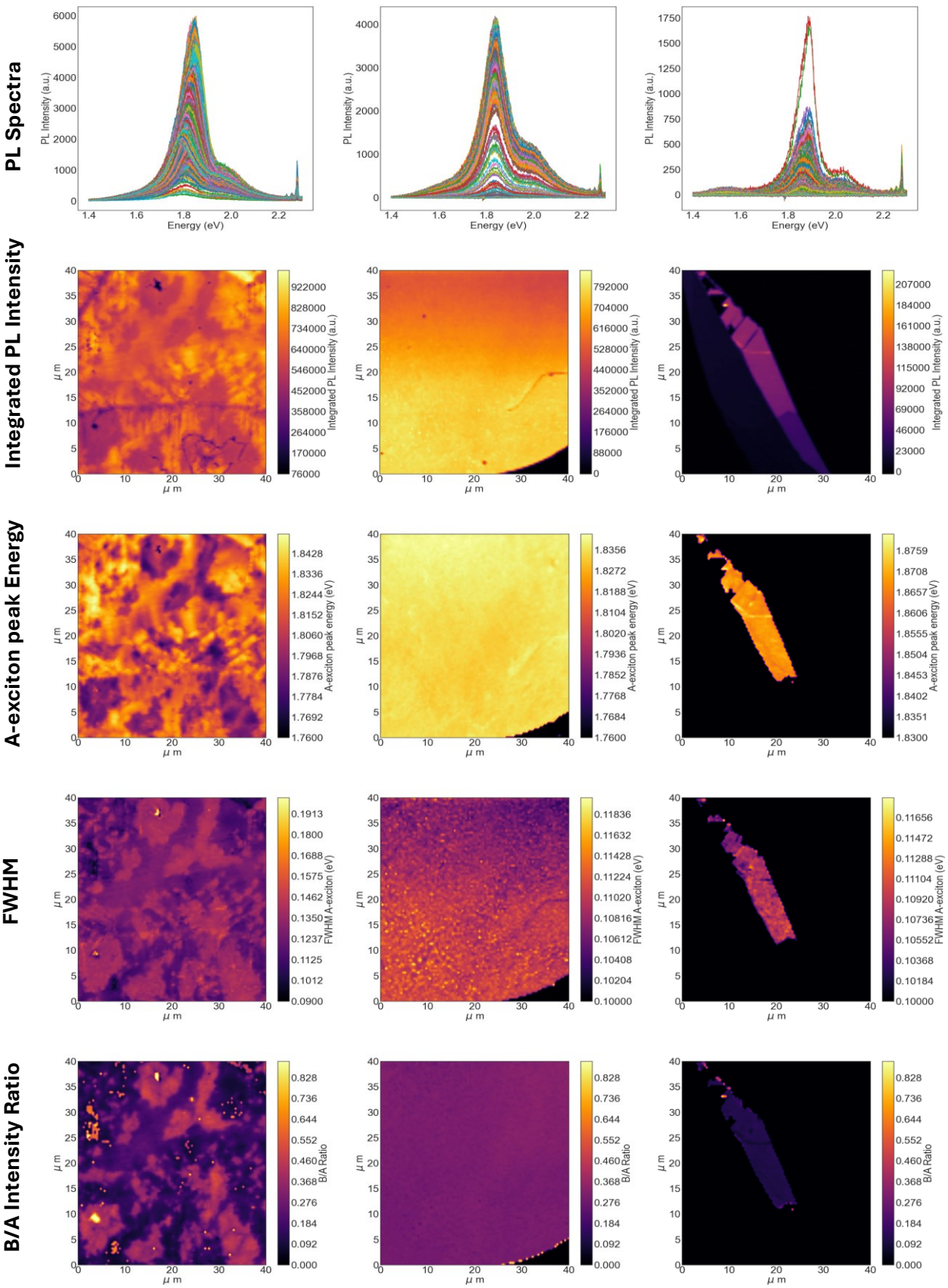

A6. PL Maps and Spectrums for CVD, GAE and PDMS samples for WS_2

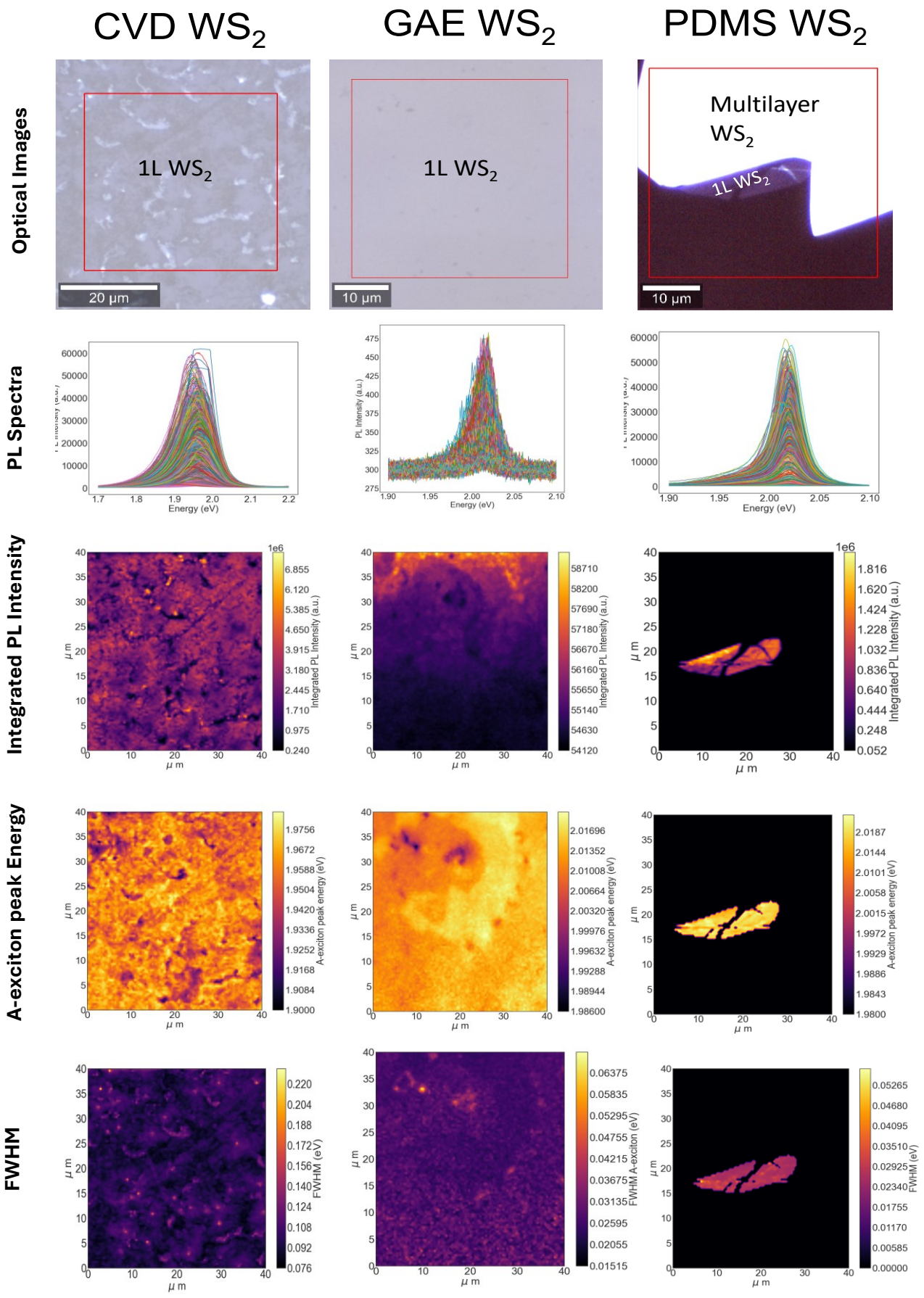

A7. Analysis of PL and Raman spectra for ReS_2

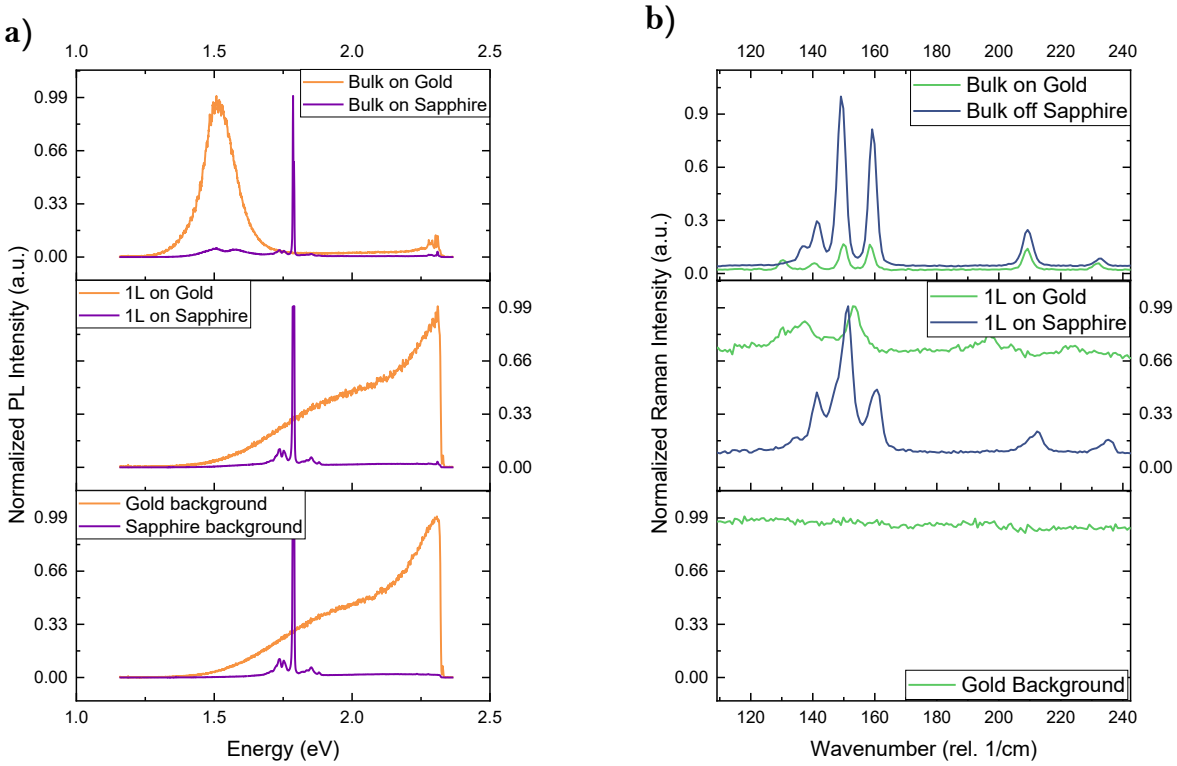

Figure A7: **a)** PL spectra for ReS_2 on (*orange*) and off (*violet*) gold; **b)** Raman spectra for ReS_2 on (*green*) and off (*blue*) gold.

A8. Different Methods Tried for Gold-Assisted Exfoliation

Table 3.1: Summary of different methods attempted. Here "ML" refers to monolayer in general.

Attempt	Aim	Parameters/Conditions	Layer Sequence After Etching	Outcome	Description	Important Learnings
1	Etch Au and retain ML	• Spin-coated PMMA of 120,000 Mol. W with 2.5% wt/vol in Toluene. • Substrate: Si/SiO_2	*PMMA-ML-Au-Epoxy-Si/SiO₂*	Failed to retain ML	ML was swept away during Au etching, although some areas showed coexistence of ML and Au layers.	PMMA of 120,000 Mol. W with 2.5% wt/vol in Toluene is too dense to allow easy passage of the etchant.
2	Exfoliate ML on Au by replacing Epoxy	• Substrate: Si/SiO_2		Failed template stripping of Au foil on Si/SiO_2 substrate		
3	Etch Au through epoxy and	• Spin-coated PMMA of 120,000 Mol. W	*PMMA-ML-Au-Epoxy*	Failed to retain ML	Same as attempt 1 but without	

	retain ML	with 2.5% wt/vol in Toluene • Substrate: Si/SiO_2			Si/SiO_2 substrate.	
4	Etch Au and retain ML	• Spin-coated PMMA of 120,000 Mol. W with 0.5% wt/vol in Toluene • Substrate: Si/SiO_2	*PMMA-ML-Epoxy-Si/SiO₂ substrate*	Successfully retained ML and removed Au but failed to retain the *Au-ML* configuration	ML stuck to epoxy, making analysis and transfer difficult.	Epoxy is unsuitable for transferring the monolayer and interferes with obtaining the PL signal.
5	Exfoliate ML using TRT	• Spin-coated PVP of 10% wt/vol in Toluene • Substrate: Si/SiO_2		Failed to exfoliate ML on *Au-TRT*	Surface roughness compromised contact between ML and Au layer.	PVP layer is too thin to compensate for surface roughness of the TRT, affecting the smoothness of the gold foil.
6	Exfoliate ML using TRT	• Spin-coated PMMA of 120,000 Mol. W with 10% wt/vol in Toluene • Substrate: Si/SiO_2		Failed to exfoliate ML on *Au-TRT*	Same as attempt 5 but with reduced surface roughness.	Increasing PMMA concentration can further reduce surface roughness and act as a spacer layer between the gold foil and TRT.
7	Exfoliate ML using TRT	• Spin-coated PMMA of 950,000 Mol. W with 8% wt/vol in anisole. • Substrate: Si/SiO_2		Successfully exfoliated ML on *Au-TRT* but failed to retain the *Au-ML* configuration	Au-foil detached from Si/SiO_2 substrate due to surface roughness and contamination upon treatment with Acetone to remove the PMMA.	Al_2O_3 substrates with better surface smoothness may help in keeping the Au foil attached during PMMA removal the process.
8	Exfoliate ML using TRT	• Spin-coated PMMA of 950,000 Mol. W with 8% wt/vol in anisole. • Substrate: Al_2O_3	*ML-Al₂O₃ substrate*	Successfully exfoliated ML on *Au-TRT* and successfully etched the Au foil and retained the monolayer on sapphire substrates		The method is reliably reproducible and can also be further used to fabricate the heterostructures